Final Report

to

Dr. Todd Steiner
Air Force Office of Scientific Research

Order Lattices of Quantum Dots

AFOSR Program #F49620-01-1-0311

for the period

September 1, 2001 – June 30, 2004

James S. Speck
and
Pierre M. Petroff

Materials Department
University of California
Santa Barbara, CA 93106

20041119 039

1

REPORT DOCUMENTATION PAGE

AFRL-SR-AR-TR-04-

0574

data needed, and completing and reviewing this collection of information. Send comments regarding this burden estimate or any oth
this burden to Department of Defense, Washington Headquarters Services, Directorate for Information Operations and Reports (0704
4302. Respondents should be aware that notwithstanding any other provision of law, no person shall be subject to any penalty for fa
valid OMB control number. **PLEASE DO NOT RETURN YOUR FORM TO THE ABOVE ADDRESS.**

1. REPORT DATE (DD-MM-YYYY)	2. REPORT TYPE	3. DATES COVERED (From - To)
November 1, 2004	Final	04/15/2001 – 06/30/2004

4. TITLE AND SUBTITLE
Ordered Lattices of Quantum Dots

5a. CONTRACT NUMBER

5b. GRANT NUMBER
F49620-01-1-0311

5c. PROGRAM ELEMENT NUMBER

6. AUTHOR(S)
James S. Speck
Pierre M. Petroff

5d. PROJECT NUMBER

5e. TASK NUMBER

5f. WORK UNIT NUMBER

7. PERFORMING ORGANIZATION NAME(S) AND ADDRESS(ES)

8. PERFORMING ORGANIZATION REPORT NUMBER

9. SPONSORING / MONITORING AGENCY NAME(S) AND ADDRESS(ES)
USAF, AFRL
AFOSR
4015 Wilson Blvd, Room 713
Arlington, VA 22203-1954

10. SPONSOR/MONITOR'S ACRONYM(S)

11. SPONSOR/MONITOR'S REPORT NUMBER(S)

12. DISTRIBUTION / AVAILABILITY STATEMENT

Distribution Statement A: unlimited

13. SUPPLEMENTARY NOTES

14. ABSTRACT
This program has been focused on the development of the enabling tools for future generation optoelectronic devices. We have focused on two main areas: (i) controlled position of quantum dots – primarily in the InAs/GaAs system and (ii) development of group III-nitride quantum dots – primarily in the GaN/AlN system. In the first area, we achieved mesa lattices in GaAs with low densities of single InAs quantum dots on a fraction of the mesa tops. In the second area, we have developed a comprehensive understanding of GaN quantum dot growth by rf plasma MBE. We have controlled quantum dot densities in the range $10^8 - 10^{11}$ cm^{-2}, and we have extensively characterized the optical properties of the dots by both pumping the dots or defect states in the matrix and by illuminating the matrix with above gap radiation.

15. SUBJECT TERMS

16. SECURITY CLASSIFICATION OF:			17. LIMITATION OF ABSTRACT	18. NUMBER OF PAGES	19a. NAME OF RESPONSIBLE PERSON
a. REPORT	b. ABSTRACT	c. THIS PAGE			19b. TELEPHONE NUMBER (include area code)

Standard Form 298 (Rev. 8-98)
Prescribed by ANSI Std. Z39.18

Objectives

This program has been focused on the development of the enabling tools for future generation optoelectronic devices. We have focused on two main areas: (i) controlled position of quantum dots – primarily in the InAs/GaAs system and (ii) development of group III-nitride quantum dots – primarily in the GaN/AlN system.

Summary of Key Findings

We provide a brief summary of the main results of our work and where possible, include the resulting publication from the work as an Appendix.

High Temperature Luminescence from GaN Quantum Dots

In our early work on GaN quantum dots embedded in an AlN matrix, grown by plasma-assisted molecular beam epitaxy (PA-MBA), we focused on the photoluminescence (PL) properties of the dots. We observed strong (PL) from the QDs from 8 to 750 K. Atomic force microscopy studies demonstrate that the QDs have diameters of (30 ± 5) nm and heights of (3 ± 1) nm. PL from the quantum dots was compared to that of a gallium nitride growth template film to unambiguously demonstrate the contribution of the QDs to the spectra. Integrated PL intensity was observed to remain strong well above 300 K, and we attribute the decrease in the quantum dot PL at higher temperatures to phonon-mediated carrier ionization of deep levels.

Full details of this work are given in the publication (provided as Appendix I):

"Temperature dependent photoluminescence of MBE grown gallium nitride quantum dots,"
J. Brown, C. Elsass, C. Poblenz, P.M. Petroff, J.S. Speck, *Phys. Stat. Sol. B* **228**, 199 (2001).

Electronic Properties of GaN Induced by a Subsurface Stressor

In conjunction with our experimental work on GaN quantum dots, we have also examined the role of quantum dots, as stressors, on the electronic properties of a III-nitride matrix. In this work, we focused on the influence of the strain field originating from a subsurface point source of dilatation (point stressor) on the electronic properties of nitride semiconductors. In the far field, real quantum dots can be viewed as such point stressors. The material surrounding the stressor was considered either to be a uniform GaN matrix or GaN matrix with an (In,Ga)N quantum well which is grown pseuodomorphically between the stressor and the free surface. Isotropic elasticity was used to find the strain field around the stressor. A **k·p** perturbation theory approach was then applied to examine the shifts of the conduction and valence band edges caused by the stressor. We found lateral confinement for electrons and holes, which could be utilized to realize a strain-induced quantum dot in the quantum well.

Details of this work are given in the publication (provided as Appendix II):

"Electronic properties of GaN induced by a subsurface stressor,"
P. Waltereit, A.E. Romanov, J.S. Speck, *Appl. Phys. Lett.* **81**, 4754 (2002).

Further details are provided in the publication (provided as Appendix III)

"Buried stressors in nitride semiconductors: influence on electronic properties,"
A.E. Romanov, P. Waltereit, and J.S. Speck, *J. Appl. Phys.*, accepted for publication.

GaN Quantum Dot Density Control by RF-Plasma-Assisted MBE

In our more recent work on GaN quantum dots, we have focused both on the QD growth mechanisms and on the control of QD density. In this work, we again have grown GaN QDs in the Stranski-Krastanov mode on AlN (0001) by rf-plasma molecular beam epitaxy at 750 °C. After depositing the equivalent of 2-3 monolayers GaN coverage, as limited by N-fluence under Ga-droplet growth conditions, excess Ga was desorbed and Stranski-Krastanov islands formed under vacuum. We determined the dependence of island density as a function of GaN coverage (for two growth rates: 0.10 and 0.23 monolayers per second), as estimated from atomic force microscopy and cross-sectional transmission electron microscopy. With a GaN growth rate of 0.23 monolayers per second, the island density was found to vary from less than 3.0×10^8 to 9.2×10^{10} cm^{-2} as the GaN coverage was varied from 2.2 (critical thickness) to 3.0 monolayers. We are the first group to realize GaN QDs with densities in the range where single dot PL studies may be possible. For a GaN growth rate of 0.10 monolayers per second, the island density varied from 2.0×10^{10} to 7.0×10^{10} cm^{-2} over a GaN coverage range of 2.0 to 3.0 monolayers. For each growth rate, the GaN islands were found to be of nearly uniform size, independent of the quantum dot density

Full details of this work are given in the publication (provided as Appendix IV):

"GaN quantum dot density control by rf-plasma molecular beam epitaxy,"
J. Brown, F. Wu, P.M. Petroff, and J.S. Speck, *Appl. Phys. Lett.* **84**, 2690 (2004).

In situ Monitoring of GaN Growth by by RF-Plasma-Assisted MBE

In conjunction with our work on detailed studies of GaN QD growth, we have been developing basic tools to monitor the surface coverages, desorption rates and related phenomena during growth. In this work we focused on the very important issue of the evolution of the Ga adlayer during plasma–assisted molecular beam epitaxy of (0001) GaN as a function of both Ga flux and growth temperature. In situ quadrupole mass spectrometry was used to quantitatively determine the adsorbed Ga coverage by monitoring its subsequent desorption after GaN growth. Independent of the growth time, the Ga adlayer was found to form steady state coverages that increase *continuously* from 0 to 2.5 monolayers when raising the Ga flux from N–rich to moderate Ga–rich growth conditions. At higher Ga fluxes or lower growth temperatures (Ga droplet regime), macroscopic Ga droplets form on top of the Ga adlayer. Based on the temperature–dependency for the transition between the Ga adlayer and Ga droplet regime we determined an apparent activation energy of 3.4 eV, which is discussed with to our own earlier work and to work of other groups (our results confirm earlier UCSB work, in collaboration with Infineon and refute claims in recent papers).

Full details of this work are given in the publication (provided as Appendix V):

"Continuous evolution of Ga adlayer coverages during plasm-assisted molecular beam epitaxy of (0001) GaN,"
G. Koblmueller, J. Brown, R. Averback, H. Riechert, P. Pongratz, J.S. Speck, *submitted for publication*.

In Situ Studies of GaN Quantum Dot Formation

We have built on our work on QMS to reveal the mechanisms of GaN quantum dot formation. Previously, we showed that GaN quantum dots could be realized by growth on (0001) AlN under Ga-rich conditions, followed by a growth interrupt, in which the the gallium wetting layer desorbs and GaN quantum dots form. We have simultaneously followed this process with reflection high energy electron diffraction (RHEED) and QMS. We have found that the GaN QDs form when the excess gallium on the surface, during desorption, is ~1 ML, as shown in Fig. 1. Details of this work will be described in a forthcoming publication.
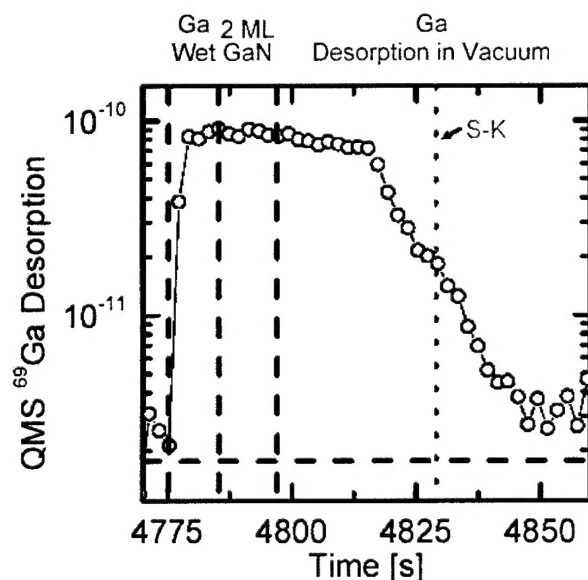

Figure 1   QMS data for GaN quantum dot formation. In this experiment, the ^{69}Ga desorption was monitored for GaN growth on (0001) AlN. First, the AlN was pre-wetted with Ga, then ~2 ML of GaN were deposited under Ga-rich conditions (Ga/N >10) and then both the Ga and N fluxes were interrupted. The GaN quantum dots (S-K transition) formed when the excess gallium coverage was ~ 1 ML (The S-K transition was monitored with RHEED).

Spectroscopy of Gallium Nitride Quantum Dots

We have continued to study details of the GaN QD PL. Our earlier studies were performed with HeCd laser (325 nm or 3.81 eV). This wavelength of radiation can neither directly pump the AlN matrix or a 1, 2, or 3 ML thick GaN wetting layer. We concluded that we were most likely pumping the dots through defect states in the AlN matrix. In the final year of the program, we extensively studied the GaN QD PL by directly pumping the AlN matrix with a recently acquired 193 nm excimer laser. We found that the overall QD PL was shifted to shorter wavelength when pumping with 193 nm radiation in comparison with when pumping with 325 nm radiation, as shown in Fig. 2. We attribute this difference in PL wavelength to the different coupling of the photogenerated carriers to the dots. Pumping the GaN/AlN sample with 325 nm radiation only allows transfer of carriers from the AlN or GaN wetting layer to the largest dots.

4

By directly pumping the AlN matrix, we have observed the 1, 2, and 3 ML thick GaN wetting layer on the AlN. To our knowledge, this is the first observation of the GaN wetting layer PL, as shown in Fig. 3. We have found that the thickness of the GaN wetting layer scales directly with the total GaN deposition. Additionally, we have found that the thickness of the wetting layer scales inversely with the excess Ga flux during the GaN deposition. We attribute this latter trend to reduced organization time for dots to form during the excess Ga desorption and thus more GaN forms as wetting layer as opposed to dots. A full manuscript will be prepared that addresses our recent PL studies.
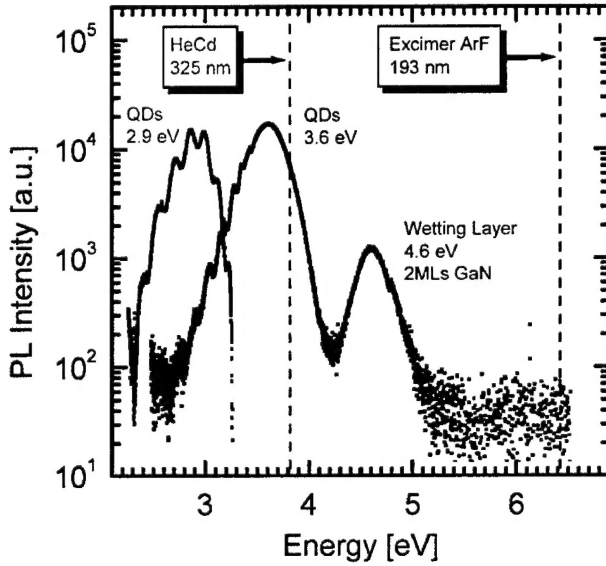
Figure 2   GaN QD PL with different pump wavelengths. Pumping with 325 nm light results in only relatively long wavelength PL from the dots. Pumping with 193 nm light shows that the average QD PL is at higher energy and also facilitates the observation of the GaN wetting layer PL.
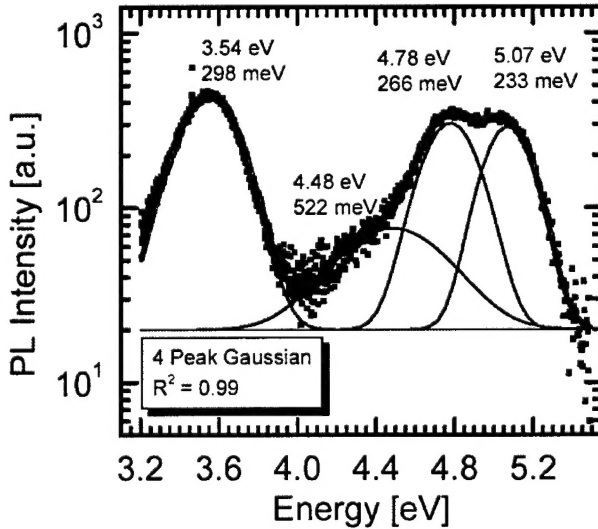
Figure 3   GaN QD PL for an intermediate density sample (QD density 2×10^{10} cm^{-2}) pumped with 193 nm light. The GaN QD PL is centered at 3.54 eV. PL peaks at 5.07 ev, 4.78 eV, and 4.48 eV correspond to 1, 2, and 3 ML thick GaN wetting layers. The position of the wetting layer luminescence is in close agreement with self-consistent Schrodinger-Poisson calculations for the energy difference of the ground states of the quantum well.

Quantum Dot Lattices

In this program, we also made great progress in the growth of low density InAs quantum dot samples on periodic mesa stressor lattices. The specific goal of this work was to place single dots at controlled locations in the defect sites of photonic bandgap crystals. Controlled dot location will in defect lattices will facilitate single quantum dot optoelectronic devices.

The mesa stressor lattices are formed by holographic lithography of a GaAs wafer; followed by chemical etching and MBE regrowth of a GaAs buffer layer; growth of an InGaAs stressor layer and second GaAs buffer; followed by growth of InAs quantum dots. During this period, we have realized low densities of single dots on the mesa lattice tops, as shown below in Fig. 4.
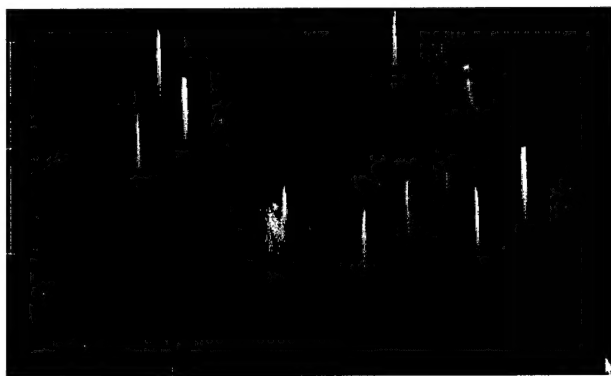

Figure 4 AFM perspective showing single InGaAs quantum dots on a InGaAs/GaAs stressor mesa lattice. The mesa lattice period is ~0.65 μm and the lattice is aligned along the GaAs <110> directors.

Capped low density multilayer samples showed strong PL emission and clearly resolvable features associated with the s, p, and d shells. On annealed samples, we have observed single dot emission. The realization of strong PL reflects our effort to optimize all steps of the processing and regrowth procedure. In the next reporting period (final report for the current project) we will present results on the successful incorporation of single dots in the defect sites of photonic bandgap structures.

The work on controlled position has continued with Prof. Petroff and is an enabler for a range of programs in his group and in the groups of Prof. Evelyn Hu and others at UCSB.

Personnel Supported

Antonio Badolato – Graduate Student Researcher, Electrical and Computer Engineering
Jay Brown - Graduate Student Researcher, Materials Department
Dr. Alexei Romanov – visiting faculty, Materials Department
Professor Pierre Petroff – Materials Department
Professor James Speck – Materials Department

Publications

"Temperature dependent photoluminescence of MBE grown gallium nitride quantum dots,"
J. Brown, C. Elsass, C. Poblenz, P.M. Petroff, J.S. Speck, *Phys. Stat. Sol. B* **228**, 199 (2001).

"Electronic properties of GaN induced by a subsurface stressor,"
P. Waltereit, A.E. Romanov, J.S. Speck, *Appl. Phys. Lett.* **81**, 4754 (2002).

"Epitaxial Growth and Electronic Structure of Self-Assembled Quantum Dots,"
P.M. Petroff, *Topics Appl. Phys.* **90**, 1 (2003).

"GaN quantum dot density control by rf-plasma molecular beam epitaxy,"
J. Brown, F. Wu, P.M. Petroff, and J.S. Speck, *Appl. Phys. Lett.* **84**, 2690 (2004).

"Buried stressors in nitride semiconductors: influence on electronic properties,"
A.E. Romanov, P. Waltereit, and J.S. Speck, *J. Appl. Phys.*, accepted for publication.

"Self-assembling nanoparticles into holographic nanopatterns,"
S.H. Lee F.S. Diana, A. Badolato, P.M. Petroff, and E.J. Kramer, *J. Appl. Phys.* **95**, 5922 (2004).

"Square-lattice photonic crystal microcavities for coupling to single InAs quantum dots,"
K. Hennessy, C. Reese, A. Badolato, C.F. Wang, A. Imamoglu, P.M. Petroff, E. Hu, G. Jin, G. Shi, and D.W. Prather, *Appl. Phys. Lett.* **83**, 3650 (2003).

"Continuous evolution of Ga adlayer coverages during plasm-assisted molecular beam epitaxy of (0001) GaN,"
G. Koblmueller, J. Brown, R. Averback, H. Riechert, P. Pongratz, J.S. Speck, *submitted for publication.*

Appendices

Appendix I
"Temperature dependent photoluminescence of MBE grown gallium nitride quantum dots,"
J. Brown, C. Elsass, C. Poblenz, P.M. Petroff, J.S. Speck, *Phys. Stat. Sol. B* **228**, 199 (2001).

Appendix II
"Electronic properties of GaN induced by a subsurface stressor,"
P. Waltereit, A.E. Romanov, J.S. Speck, *Appl. Phys. Lett.* **81**, 4754 (2002).

Appendix III
"Buried stressors in nitride semiconductors: influence on electronic properties,"
A.E. Romanov, P. Waltereit, and J.S. Speck, *J. Appl. Phys.*, accepted for publication.

Appendix IV
"GaN quantum dot density control by rf-plasma molecular beam epitaxy,"
J. Brown, F. Wu, P.M. Petroff, and J.S. Speck, *Appl. Phys. Lett.* **84**, 2690 (2004).

Appendix V
"Continuous evolution of Ga adlayer coverages during plasm-assisted molecular beam epitaxy of (0001) GaN,"
G. Koblmueller, J. Brown, R. Averback, H. Riechert, P. Pongratz, J.S. Speck, *submitted for publication*.

Appendix I

Temperature Dependent Photoluminescence of MBE Grown Gallium Nitride Quantum Dots

J. Brown[1]), C. Elsass, C. Poblenz, P. M. Petroff, and I. S. Speck

Materials Department, University of California at Santa Barbara, Santa Barbara, CA, USA

We report on the growth and optical properties of gallium nitride quantum dots (QDs) grown by plasma-assisted molecular beam epitaxy. We have observed strong photoluminescence (PL) from the QDs from 8 to 750 K. Atomic force microscopy studies demonstrate that the QDs have diameters of (30 ± 5) nm and heights of (3 ± 1) nm. PL from the quantum dots was compared to that of a gallium nitride growth template film to unambiguously demonstrate the contribution of the QDs to the spectra. Integrated PL intensity was observed to remain strong well above 300 K, and we attribute the decrease in the quantum dot PL at higher temperatures to phonon-mediated carrier ionization of deep level.

Introduction Nitride optoelectronic structures offer emission across the visible spectrum and into the ultraviolet. Due to their wide bandgaps and thermal stability, nitride devices have the possibility of high temperature operation. Nitride quantum dots (QDs) have been investigated through molecular beam epitaxy (MBE), metalorganic chemical vapor deposition (MOCVD), and by theoretical studies [1–4]. In this work, we report on temperature dependent photoluminescence (PL) of GaN QDs grown in an AlN matrix.

A strong motivation for investigating nitride QDs is that the large bandgaps and band offsets in the group III-nitrides, in comparison with the group III-arsenides, should dramatically reduce the thermal ionization of QD confined carriers into the barrier material [4, 5]. In group III-arsenide QDs, carrier thermal ionization into the barrier was shown to be a dominant process at temperatures above 150 K [6]. In this work, phonon-mediated non-radiative carrier recombination is proposed as a dominant mechanism for the thermally induced loss of luminescent recombination above 300 K in GaN/AlN QDs.

Experiments and Results Plasma-assisted MBE has been used to grow GaN quantum dots in an AlN matrix. The following structure was grown: sapphire (0001) substrates with 0.3 µm MOCVD-grown GaN were used as templates for a 30 nm GaN buffer, followed by a partially relaxed 0.3 µm AlN buffer layer grown at 750 °C. The AlN was grown under metal-rich conditions near the cross-over to form metal droplets on the surface [7]. After deposition of each AlN layer, a 60 s delay under N flux was utilized to ensure the incorporation of any residual Al, followed by a 60 s delay with all shutters closed. Next, a stack of ten layers of GaN QDs was grown at 750 °C in the Stranski-Krastanov (S-K) growth mode [8]. To ensure adequate Ga incorporation, the Ga/N

---

[1]) Corresponding author; e-mail: jsbrown@engineering.ucsb.edu

flux ratio was set such that the GaN growth took place just inside the Ga droplet regime [7]. After opening both the Ga and N shutters for 15 s (8 Å of GaN growth), the shutters were then closed and the appearance of islands at the surface was observed in the RHEED transition ((1×1) changed from streaky to spotty) from 2D to 3D during a 20 s interval. After island formation, a 30 nm AlN capping layer was deposited to form QDs. Finally, a layer of GaN islands was grown on the surface and left uncapped for subsequent atomic force microscopy (AFM) studies.

Tapping mode AFM and temperature dependent PL from 8 to 750 K were used for sample characterization. Three separate structures were characterized in this work: the MOCVD-grown GaN on sapphire template; a partially relaxed (0.3 μm) AlN layer on the MOCVD-grown GaN on sapphire template; and the QD heterostructure described above.

The PL experiments were performed by optical pumping with a 325 nm He–Cd laser (cw). Low (8–300 K) temperature measurements were carried out with the sample attached to a liquid He cooled cryostat, while high (300–750 K) temperature measurements were performed with the same excitation power by replacing the cryostat with a hot plate.

The uncapped GaN islands exhibited a diameter of (30 ± 5) nm and a height of (3 ± 1) nm as shown in Fig. 1a. Figure 1b shows a reference 0.3 μm partially relaxed AlN film on MOCVD-grown GaN/sapphire template, which clearly shows cracking. Figure 1c is a 1×1 μm^2 scan of the same AlN reference film exhibiting spiral hillocks between the cracks, providing a locally continuous stressor film for QD nucleation.

The low temperature PL spectrum (50 K) shows a sharp peak at 3.50 eV near the band edge of GaN attributed to the bulk GaN buffer and a very broad (453 meV FWHM) peak centered at 2.76 eV which is attributed to the GaN QD as shown in Fig. 2a[2]). Theoretical studies including strain and polarization-related electric field effects predict a QD recombination of approximately 2.85 eV for 3 nm GaN/AlN QD height in reasonable agreement between the measured and calculated QD emission for the size of QDs grown for these experiments [4]. The disagreement between the model and experimental results for the QD PL include the lack of QD size resolution of the AFM, as well as the absence of a constraining AlN cap on GaN islands on the surface increasing the probability of QD ripening after the growth. Comparison of the QD PL with the growth template PL at low temperature in Fig. 2a indicates that the 2.2 eV
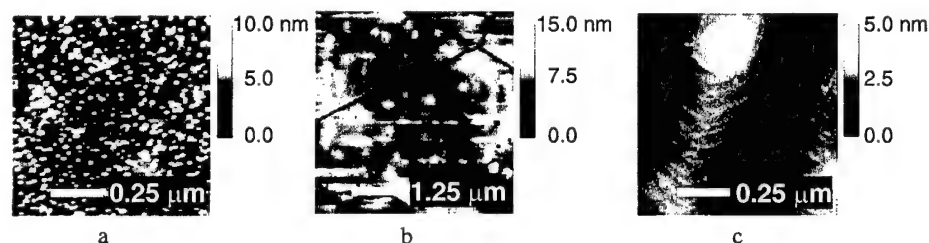

Fig. 1. Tapping mode AFM. a) GaN islands on AlN surface of ten layer GaN QD structure; b) 5×5 μm^2 scan: 300 nm partially relaxed AlN on MOCVD-grown GaN template; c) 1×1 μm^2 scan: 300 nm partially relaxed AlN, exhibiting step-flow growth between large scale surface fissures

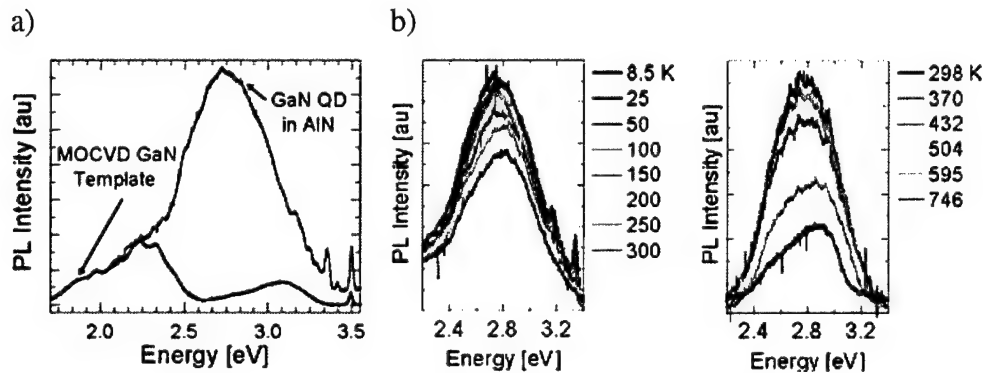[2]) Colour figure is published online (www.physica-status-solidi.com).

a)

b)

Fig. 2 (colour). a) Low temperature (50 K) PL (in arb. units) of GaN QD in AlN matrix and MOCVD-grown GaN on sapphire template. b) PL vs. temperature: low temperature (8.5–300 K) and high temperature (298–746 K) PL of GaN QD in AlN matrix

yellow luminescence is the origin of the low energy shoulder of the QD peak. The donor–acceptor emission, centered at 3.1 eV, was not observed above 100 K, allowing the observed emission at 2.76 eV to be attributed to GaN QDs.

Temperature dependent PL from 8.5 to 746 K was observed in the GaN/AlN QD heterostructure, as shown in Fig. 2b. The QD PL intensity was observed to remain strong well above room temperature. A blue shift of the QD emission with increasing temperature was observed, as shown in Fig. 2b, indicating a preferential loss of carriers from larger QDs.

Excluding the template yellow luminescence, an Arrhenius plot of the integrated luminescence intensity of the QD emission is shown in Fig. 3a. An activation energy for exciton concentration under steady state conditions as a function of temperature of (46 ± 2) meV was determined from the Arrhenius plot [6, 9].

a)

b)

$$PL(T) = \frac{A}{Be^{\frac{-E_A}{k_B T}} + 1}$$

■ Integrated PL Intensity
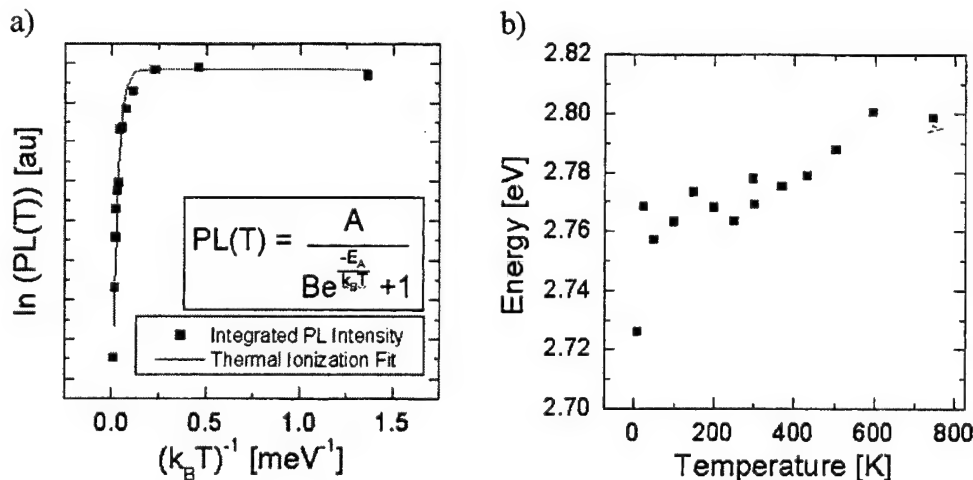— Thermal Ionization Fit

Fig. 3. Photoluminescence as a function of temperature. a) Arrhenius plot of integrated QD PL intensity. b) QD emission energy vs. temperature

Due to the small value of the experimentally determined activation energy, in contrast with the relatively large thermal ionization barriers predicted for this structure [4], the PL decrease mechanism is proposed to be phonon mediated non-radiative recombination. In this process, deep levels in the AlN barrier are thermally ionized, creating non-radiative recombination centers for QD carriers. Polarization-related electric fields cause carrier separation in GaN/AlN QDs, in which electrons are localized near the QD tops and holes are localized in the wetting layer immediately below the QD [4]. The spatial separation of carriers is proposed to enhance the loss of carriers from the QDs to ionized traps, preferentially in larger QDs because carrier separation is expected to be proportional to QD size. The proposed mechanism provides a qualitative explanation for the observed blue shift of QD PL with increasing temperature. Further work is underway to verify this model for the loss in QD luminescence at high temperature.

Conclusion In conclusion, GaN/AlN QDs have been shown to display unique high temperature luminescent behavior. The spontaneous and strain induced polarization complicates the analysis of carrier loss mechanisms in GaN/AlN QD heterostructures, but the promise of high temperature optoelectronics applications necessitates further investigation of these phenomena.

References

[1] F. Widmann, B. Daudin, G. Feuillet, Y. Samson, J. L. Rouvière, and N. Pelekanos, J. Appl. Phys. **83**, 7618 (1998).
[2] B. Damilano, N. Grandjean, F. Semond, J. Massies, and M. Leroux, Appl. Phys. Lett. **75**, 962 (1999).
[3] S. Tanaka, S. Iwai, and Y. Aoyagi, Appl. Phys. Lett. **69**, 4096 (1996).
[4] A. D. Andreev and E. P. O'Reilly, Phys. Rev. B **62**, 15851 (2000).
[5] A. Rizzi, R. Lantier, F. Monti, H. Luth, F. Della Sala, A. Di Carlo, and P. Lugli, J. Vac. Sci. Technol. B **17**, 1674 (1999).
[6] S. Fafard, S. Raymond, G. Wang, R. Leon, D. Leonard, S. Charbonneau, J. L. Merz, P. M. Petroff, and J. E. Bowers, Surf. Sci. **361/362**, 778 (1996).
[7] B. Heying, R. Averbeck, L. F. Chen, E. Haus, H. Riechert, and J. S. Speck, J. Appl. Phys. **88**, 1855 (2000).
[8] D. J. Eaglesham and M. Cerullo, Phys. Rev. Lett. **64**, 1943 (1990).
[9] G. Bacher, H. Schweizer, J. Kovac, and A. Forchel, Phys. Rev. B **43**, 9312 (1991).

Appendix II

Electronic properties of GaN induced by a subsurface stressor

P. Waltereit, A. E. Romanov,[a] and J. S. Speck[b]

Materials Department, University of California, Santa Barbara, California 93106

The influence of the strain field originating from a subsurface point source of dilatation (point stressor) on the electronic properties of nitride semiconductors is investigated. In the far field, real quantum dots can be viewed as such point stressors. The material surrounding the stressor was considered either to be a uniform GaN matrix or GaN matrix with an (In,Ga)N quantum well which is grown pseudomorphically between the stressor and the free surface. Isotropic elasticity was used to find the strain field around the stressor. A $\mathbf{k} \cdot \mathbf{p}$ perturbation theory approach was then applied to examine the shifts of the conduction and valence band edges caused by the stressor. We find lateral confinement for electrons and holes, which can be utilized to realize a strain-induced quantum dot in the quantum well. © *2002 American Institute of Physics.* [DOI: 10.1063/1.1524300]

The effects of a stressor, i.e., a source of mechanical strains and stresses, on electronic properties of homogeneous layers and quantum wells (QWs) have been explored in recent studies of QDs.[1–3] In the case of zincblende structures, Davies[1] investigated both surface and subsurface stressors but neglected the presence of hydrostatic strain induced by a stressor in a semi-infinite medium. Tulkki *et al.*[4] examined the influence of a surface stressor on the optical properties of a buried QW and obtained excellent agreement with corresponding experiments by Lipsanen *et al.*[5] More recently, Andreev *et al.*[6] studied wurtzite GaN/AlN QDs in detail and reported on the relationship between the shape and size of the dot and confined wave functions in the dot. In this letter, we report on the influence of the strain field originating from a subsurface point dilatation stressor (which can approximate a real QD in the far field) on the electronic properties of wurtzite nitride semiconductors. The material surrounding the stressor is considered either to be a uniform GaN matrix [see Fig. 1(a)] or a GaN/(In,Ga)N/GaN single QW (SQW) which is grown pseudomorphically between the stressor and the free surface [see Fig. 1(c)]. We use a $\mathbf{k} \cdot \mathbf{p}$ perturbation theory approach to examine the shifts of the conduction and valence band edges caused by the stressor. We do not include the effects of electrostatic fields induced by polarization fields.

In our model, see Fig. 1(a), the point dilatation stressor is located at $r = (x^2 + y^2)^{1/2} = 0$ and $z = h$. The $z = 0$ plane is taken as the (0001) sample surface. In general, the elastic properties of a medium are anisotropic and the stressor may have arbitrary shape and size leading to complex strain fields in close vicinity to the stressor, thus, requiring rather elaborate analytical or finite-element method (FEM) calculations (see, e.g., Refs. 3, 7, and 8). To simplify the model and proceed with analytically tractable results, the following approximations were employed: (i) the same elastic constants for (In,Ga)N as for GaN and (ii) isotropic elasticity with averaged Poisson ratio and shear modulus. It is likely (see,

e.g., Ref. 7) that these simplifications underestimate the magnitude of the hydrostatic strain present around the dot.

The effect of point dilatation stressor can be compared with those of a QD of volume V and having crystal lattice mismatch (characterized by misfit parameter f) with respect to the surrounding matrix. In the far field, a real QD can be replaced by a singular dilatation point stressor with an effective strength $S = fV = Pd/2\mu \, (1-2\nu)/(1+\nu)$ (Refs. 9 and 10), where μ is the shear modulus and ν is Poisson ratio (see Fig. 1 for definition P and d).

The comparison of exact analytical solutions for dilatating ellipsoidal QDs or FEM calculations for cuboidal and trapezoidal QDs shows that in the far field (at distances $\ell > \ell_c \approx \sqrt[3]{V}$) strains and stresses of QDs agree well with those obtained for a dilatation point stressor.[9] Therefore, we use the solutions for the stresses $\sigma_{ij}^{\text{point}}(x,y,z)$ of a dilatation point stressor, which have simple analytical representation for both infinite and semi-infinite isotropic elastic media.[10] Using Hooke's law, one can derive the corresponding strain components $\varepsilon_{ij}^{\text{point}}$, which are also a function of the Poisson ratio ν. Since wurtzite GaN is elastically anisotropic, we choose to use an average Poisson ratio $\bar{\nu}$, which was estimated by averaging the Poisson ratios along the three Cartesian axes according to $\bar{\nu} = -\frac{1}{3}[s_{13}/s_{33} + (s_{12} + s_{13})/s_{11}]$ where s_{ij} are the elastic compliances for GaN. Using the elastic constants from Ref. 11 we obtain $\bar{\nu} = 0.234$. Here, we do not show the whole analytical expression for $\varepsilon_{ij}^{\text{point}}$, but rather we restrict ourselves to an example, namely, the hydrostatic strain field

$$\varepsilon_{\text{hydro}}^{\text{point}}(r,z) = S \frac{(1+\nu)(1-2\nu)}{\pi(1-\nu)} \frac{2(z+h)^2 - r^2}{[r^2 + (z+h)^2]^{5/2}},$$

which is plotted in Fig. 1(b). Due to the free surface, the hydrostatic strain field is *not* zero in contrast to the case of a stressor in an infinite medium (note in the general case of an anisotropic medium, the hydrostatic strain field is nonzero outside the stressor even in a infinite medium, see, e.g., Ref. 7). In addition to a homogeneous GaN matrix surrounding the subsurface stressor, we also considered a GaN/(In,Ga)N/GaN SQW grown pseudomorphically between the stressor and the free surface as schematically shown in Fig. 1(c). In

[a]Permanent address: A.F. Ioffe Physico-Technical Institute, 194021 St. Petersburg, Russia.
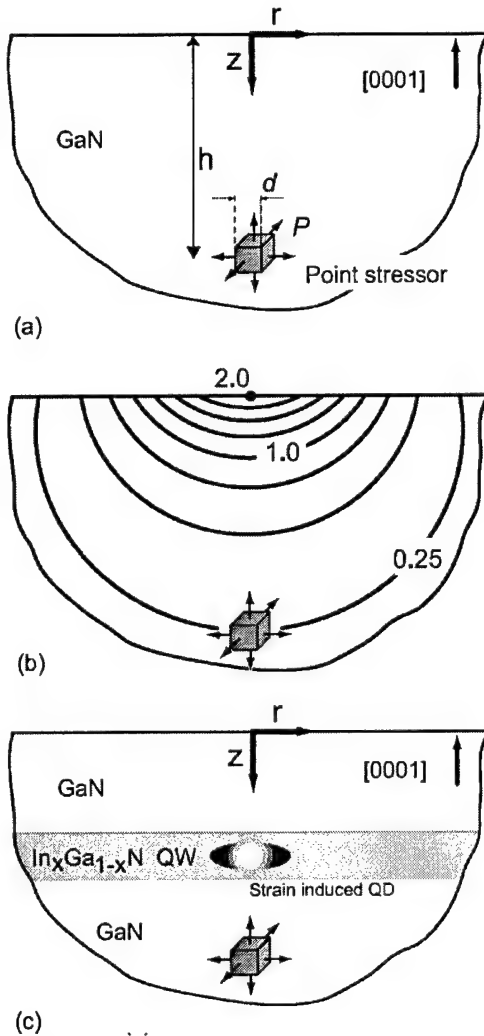[b]Electronic mail: speck@mrl.ucsb.edu

Appl. Phys. Lett., Vol. 81, No. 25, 16 December 2002

Waltereit, Romanov, and Speck   4755

FIG. 1. Subsurface stressor in GaN. (a) Schematic for a point stressor (modeling $In_yGa_{1-y}N$ QD) placed in a GaN layer. The sample surface $z=0$ corresponds to the (0001) GaN growth plane with the z axis in the $[000\bar{1}]$ crystallographic direction. The point stressor is described by three orthogonal force dipoles with separation d and magnitude P acting on the faces of a cube with volume d^3 in the limit of $d \to 0$. (b) Hydrostatic strain $\varepsilon_{hydro}^{point}(r,z)$ induced by the point stressor placed at the distance h from the free surface of an isotropic half-space. The strain is given in units of $S/\pi h^3 (1+\nu)(1-2\nu)/(1-\nu)$, where $S=fV$ is the effective strength of the stressor and ν is Poisson ratio. The contour lines are spaced by 0.25. (c) Schematic for a point stressor placed in a GaN layer and an additional $In_xGa_{1-x}N$ QW grown pseudomorphically between the point stressor and the free surface.

this case, the total strain field ε_{ij}^{total} is simply given by the *linear* superposition $\varepsilon_{ij}^{point} + \varepsilon_{ij}^{QW}$ where ε_{ij}^{QW} is the strain field associated with lattice mismatch of the SQW. In contrast to the strain field, the shift of the electron and hole energies is *nonlinear* with strain as these energies represent the eigenvalues of a (6×6) Hamiltonian in the $\mathbf{k} \cdot \mathbf{p}$ calculations.[12,13]

In unstrained wurtzite GaN, there are three closely spaced top valence bands (VBs) at the Brillouin-zone center, usually referred to as heavy-hole (HH), light-hole (LH), and crystal-field split-off hole (SCH). Due to strain, both the CB and the VB states are modified leading to shifts of the corresponding band edges relative to their values for unstrained material. To estimate the strain-induced shifts, we use the $\mathbf{k} \cdot \mathbf{p}$ perturbation approach developed by Bir and Pikus[12] em-
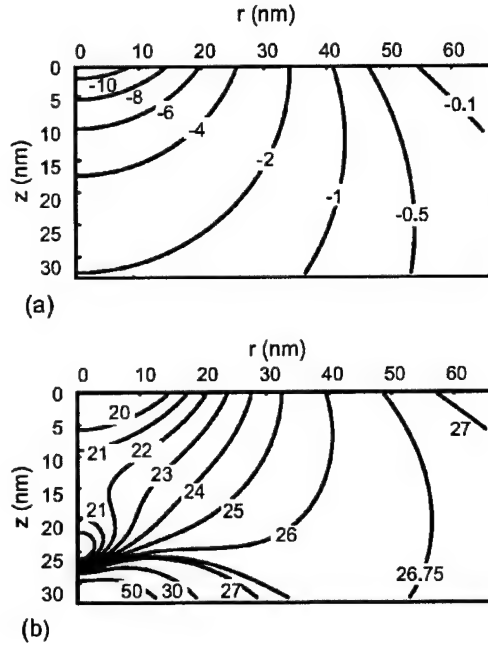

FIG. 2. Change in the GaN conduction and valence band energies caused by the subsurface stressor. (a) Map for the conduction band edge in $r-z$ coordinates. (b) Map for the VB closest to the conduction band in $r-z$ coordinates. The point stressor is located at a distance $h=41$ nm from the surface and possesses the effective strength $S=fV$ equivalent to an $In_{0.5}Ga_{0.5}N$ island with a volume of 200π nm^3 ($\ell_c \approx 8$ nm) and $f=0.0507$. The average Poisson ratio is taken as $\bar{\nu}=0.234$, the contour values are given in meV.

ploying the corresponding deformation potentials for GaN.[13] The stressor strain field leads to changes in the original VB states such that it is no longer possible to simply describe them as HH, LH, and SCH. In the following, we label the individual VBs as top, middle, and bottom VB according to their energy with the top VB being closest to the CB.

The shifts of the CB and VB energies in a GaN matrix due to the (In,Ga)N subsurface stressor are shown in Figs. 2 and 3. This type of point stressor represents an equivalent "positive" dot, i.e., the unit cell volume of the unstrained dot is larger than that of the surrounding matrix. The average lattice misfit parameter f for the positive $In_yGa_{1-y}N$ QD in GaN matrix can be defined as $f=(2f_\parallel + f_\perp)/3$, where $f_\parallel = |a_{GaN} - a_{(In,Ga)N}|/a_{(In,Ga)N}$ and $f_\perp = |c_{GaN} - c_{(In,Ga)N}|/c_{(In,Ga)N}$ are in-plane and out-of-plane lattice misfits, respectively. The in-plane (a) and out-of-plane (c) lattice constants of In_yGa_{1-y} are determined by applying Vegard rule $[a,c]_{(In,Ga)N} = y[a,c]_{InN} + (1-y) \times [a,c]_{GaN}$. For an $In_{0.5}Ga_{0.5}N$ QD and known lattice parameters for InN and GaN (Ref. 14) the average misfit f is approx. 0.0507. All data presented in Figs. 2 and 3 are calculated within the valid range of the point source approximation[9] as we do not approach the point source closer than its characteristic length ℓ_c. The shift of the CB is proportional to the hydrostatic strain,[12,13] hence, Fig. 2(a) resembles Fig. 1(b) in different units. The localization depth near the surface is around 10 meV, thus, weak electron localization is expected at room temperature. However, strong electron localization will occur at low temperature. In contrast, the top VB [Fig. 2(b)] displays a rather complex dependence on the actual location. In-plane and out-of-plane cross sections of the VB structure
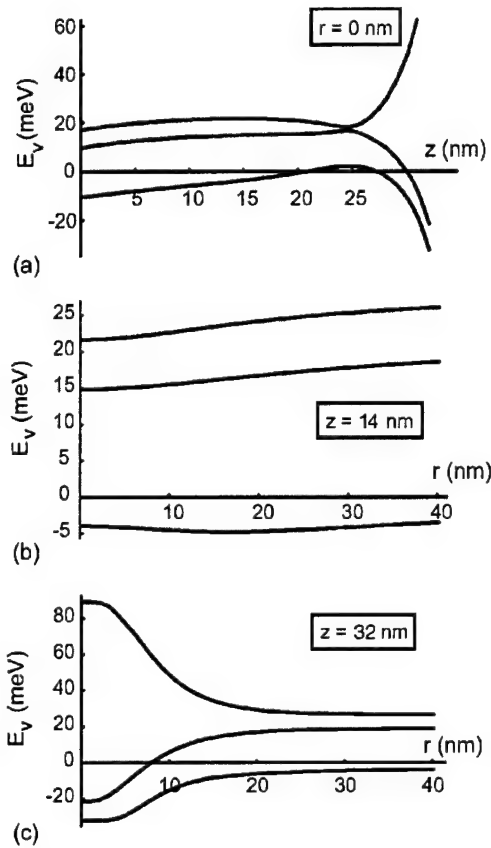
FIG. 3. Cross sections of the VB structure in GaN in the presence of the subsurface stressor. (a) VB energies dependence on depth z for $r = 0$. (b), (c) Radial dependencies for the energy of three VBs for $z = 14$ and $z = 32$ nm, respectively. The parameters of the stressor used in these plots are the same as those used in Fig. 2, thus, well within the valid range of the point source approximation.

are shown along the z axis and for two different depths z in Fig. 3(a), and Figs. 3(b) and 3(c), respectively. Near the surface, the VBs have relative separations close to the values for unstrained material, see Fig. 3(a). However, with increasing depth z, the separation of the top and middle VBs decreases until they cross (at $z \approx 25$ nm for the parameters used for Figs. 2 and 3). Finally, the top VB moves toward the CB while the other two VBs bend away from the CB, maintaining their separation. As it follows from Figs. 3(b) and 3(c), for $r > h$, the VBs are only weakly affected by the presence of the stressor regardless of the depth z. Close to the sample surface [Fig. 3(b)], the relative positions of the VBs only change slightly close to the symmetry axis. When approaching the stressor, see Fig. 3(c), the top and middle VBs get closer together until they finally split.

The potentials calculated may have a substantial impact on excess carriers. In a homogeneous GaN matrix, electrons will always be trapped at the origin whereas holes will drift away from or towards the z axis, depending if they are generated close to the surface or close to the stressor. Hence, the overlap of the electron and hole wave functions will be rather low, leading to prolonged radiative decay times and low internal quantum efficiencies. It is interesting to consider the case of a GaN/(In,Ga)N/GaN SQW which will provide ver-

tical confinement of the carriers, namely, electron and hole confinement at the upper and lower heterointerface due to the QCSE, respectively. The total strain field $\varepsilon_{ij}^{total} = \varepsilon_{ij}^{point} + \varepsilon_{ij}^{QW}$ was used as input for the Hamiltonian in the $\mathbf{k \cdot p}$ calculations. We obtained a CB potential exhibiting lateral electron confinement at $r = 0$ regardless of the actual depth of the quantum well. However, holes will be either trapped away or at $r = 0$ depending on the actual location of the well. Therefore, we identify two important possibilities. For a shallow well close to the surface, electrons and holes show significant laterally separation and thus would have low recombination rates. However, for a QW sufficiently close to the stressor (e.g., at $z = 30$ nm for an equivalent QD placed at $h = 41$ nm as in Figs. 2 and 3), both electrons and holes are trapped at $r = 0$ in such a way that they are spatially localized resulting in a strain-induced QD inside the QW. Hence, the carriers are confined away from nonradiative recombination centers, thus, allowing for higher internal quantum efficiencies. Futhermore, the density of states near the VB maximum is substantially reduced due to the strong splitting of the top and the other two VBs.

In conclusion, we have shown that the strain field of a subsurface stressor has substantial impact on the electronic properties of wurtzite nitride semiconductors. The shifts of the CBs and VBs as obtained from a $\mathbf{k \cdot p}$ perturbation theory approach provide lateral confinement for electrons and holes, which can be utilized in order to realize strain-induced QDs in a SQW.

[1] J. H. Davies, Appl. Phys. Lett. 75, 4142 (1999).
[2] W. V. Schoenfeldt, C. Metzner, E. Letts, and P. M. Petroff, Phys. Rev. B 63, 205319 (2001).
[3] B. Jogai, J. Appl. Phys. 90, 699 (2001).
[4] J. Tulkki and A. Heinämäki, Phys. Rev. B 52, 8239 (1995).
[5] H. Lipsanen, M. Sopanen, and J. Ahopelto, Phys. Rev. B 51, 13868 (1995).
[6] A. D. Andreev and E. P. O'Reilly, Phys. Rev. B 62, 15851 (2000).
[7] E. Pan and B. Yang, J. Appl. Phys. 90, 6190 (2001).
[8] F. Glas, J. Appl. Phys. 90, 3232 (2001).
[9] A. E. Romanov, G. E. Beltz, W. T. Fischer, P. M. Petroff, and J. S. Speck, J. Appl. Phys. 89, 4523 (2001).
[10] T. Mura, Micromechanics of Defects in Solids (Martinus Nijhoff, Boston, 1987).
[11] K. Kim, W. R. L. Lambrecht, and B. Segall, Phys. Rev. B 56, 7018 (1997).
[12] G. L. Bir and G. E. Pikus, Symmetry and Strain Induced Effects in Semiconductors (Wiley, New York, 1974).
[13] We use $\alpha_{\parallel} = \alpha_{\perp} = -44.5$ eV, $\Delta_1 = 0.022$ eV, $\Delta_2 = \Delta_2 = 0.005$ eV, $D_1 = -41.4$ eV, $D_2 = -33.3$ eV, $D_3 = 8.2$ eV, $D_4 = -4.1$ eV, $D_5 = -4.7$ eV [from: S. Ghosh, P. Waltereit, O. Brandt, H. T. Grahn, and K. H. Ploog, Phys. Rev. B 65, 075202 (2002) and references therein] and $D_6 = (D_3 + 4 D_5)/\sqrt{2}$ [from: S. L. Chuang and C. S. Chang, Phys. Rev. B 54, 2491 (1996), and references therein].
[14] The lattice constants for InN and GaN are $a_{InN} = 0.354$ nm, $c_{InN} = 0.5705$ nm, and $a_{GaN} = 0.3189$ nm, $c_{GaN} = 0.5185$ nm [see, e.g., O. Brandt, P. Waltereit, and K. H. Ploog, J. Phys. D 35, 577 (2002), and references therein].

Appendix III

Buried stressors in nitride semiconductors: influence on electronic properties

A.E. Romanov[*], P. Waltereit, and J.S. Speck

Materials Department
University of California
Santa Barbara, CA 93106

Abstract

An analysis is presented on the effect of the strain field originating from a subsurface stressor (point source of dilatation or a dilatating ellipsoidal inclusion) on the electronic properties of nitride semiconductors. With good accuracy, real quantum dots can be modeled as such stressors. We consider the following material structure design: a uniform semi-infinite GaN matrix with a buried stressor or a GaN matrix with a single (In,Ga)N quantum well which is grown pseuodomorphically between the stressor and the free surface. We utilize isotropic elasticity to determine the strain field in the structures under investigation. Then we apply a **k·p** perturbation theory approach to examine the shifts of the conduction and valence band edges caused by the stressor. We find lateral confinement for electrons and holes, which can be proposed for the realization of strain-induced quantum dots in the quantum well.

---

[*]Permanent address: A.F. Ioffe Physico-Technical Institute, 194021 St. Petersburg, Russia

I. Introduction

The distinguishing properties of nitride semiconductors include their large spontaneous polarization and large piezoelectric coefficients. In nitride-based heterostructures, discontinuities in spontaneous polarization coupled with piezoelectric generated polarization caused by lattice mismatch give rise to large internal electric fields. In addition, the effect of elastic strains is magnified by large values of the deformation potentials in nitride semiconductors. A brief comparison of GaAs and GaN parameters responsible for strain related effects is given in Table I.

In general, strain-induced phenomena have a large impact on electronic properties of semiconductors [1,2]. The conduction and valence band levels and the band gap can be modified by strain. Strain-induced piezoelectric polarization charges lead to electrostatic fields of a magnitude (MV/cm) which cannot be neglected in nitride semiconductors. In fact, strain and polarization effects may be exploited to tailor heterostuctures. Examples include two-dimensional electron gases at (Al,Ga)N/GaN interfaces and large internal electrostatic fields that give rise to the quantum-confined Stark effect (QCSE) in quantum wells. Such heterostructures have been studied in detail both experimentally and theoretically, the latter being facilitated by the symmetry of two-dimensional heterostructures [3]. However, little is known about the impact of deviations from the two-dimensional nature of heterostructures on device properties. These deviations may be either intentional, *e.g.*, (In,Ga)N quantum dots [4], surface and subsurface stressors, or unintentional, as a result of uncontrolled thickness or composition modulation in growing multiple quantum wells [5]. In this article, we investigate the influence of the intentionally non-uniform strain field originating from a subsurface stressor on the electronic properties of nitride semiconductors. The stressor is chosen either as point source of

dilatation or as dilatating ellipsoidal inclusion in order to account for both far and near field effects in tractable analytical form.

The effect of finite size of quantum dots (QDs) (nanosize inclusions) on electronic and optoelectronic properties of semiconductor materials was intensively studied during the last one-and-half decades [6,7,8]. The ultimate motivation for all of these studies was to describe and detect the confinement of the carriers (electrons and holes) in QDs. Originally the confinement was attributed to the size effect on the carrier wave functions placed in three dimensional potential boxes [2,8]. In addition, it was pointed out that due to the crystal lattice mismatch between the materials of QD and surrounding matrix, considerable elastic strains can be generated inside a QD [9,10]. Such intrinsic strains contribute to the modification of semiconductor band structure via the *deformation potentials* [1]. The influence of intrinsic strains of QDs on their electronic properties have been discussed for example in refs. [11,12,13]. On the other hand QDs generate non-uniform elastic strains in their vicinity modifying the physical properties of the matrix [14]. As earlier as at the end of 1980s it was proposed to use the non-uniform strains fields originating from *surface stressors* (Fig. 1a) for lateral confinement of excitons and carriers [15,16] in a quantum well (QW), which in turn was responsible for vertical confinement (see Fig. 1a). In these reports it was demonstrated that strain induced lateral confinement may be achieved in InGaAs/GaAs QWs resulting in red-shifted photoluminescence spectra. These and other earlier observations were summarized in ref. [17]. Later on, Tulkki *et al.* [18] examined the influence of a surface stressor on the optical properties of a buried quantum well and obtained good agreement with corresponding experiments by Lipsanen *et al.* [19].

Davies [20] and Shoenfeld *et al* [21] developed the idea that a *subsurface stressor* (Fig. 1b) could be used as a tool to modify the confinement in nearby quantum wells in the case of zincblende structures. Davies investigated both surface [24] and subsurface [22] stressors and reported spatially direct and indirect electron-hole transitions, respectively. However, Davies neglected the presence of hydrostatic strain induced by a subsurface stressor in a semi-infinite medium. Whereas the properties of QDs in wurtzite semiconductors were already addressed, see for example the comprehensive paper by Andreev *et al.* [25] on the relation between the shape and size of the dot in GaN/AlN system and confined wave functions in the dot, their possible role as a subsurface stressor was not investigated. In this paper we present the development of our model for the subsurface stressors in nitride semiconductors originally proposed in ref. [26].

An important part of the analysis of strain-induced effects relies on modeling the stressor itself, *i.e.* the elastic fields produced by stressor. A number of recent studies have addressed the elasticity problems for QDs, *i.e.* stressors, of various shape, for various crystal symmetries (zinc blende and wurtzite semiconductors) including the anisotropy of material properties [31,32,33,34]. The effect of coupling electric and elastic fields generated by QDs in the materials with piezo-electric response was also studied [35]. In this paper we do not include the anisotropy of the material under investigation and do not examine complex dot geometries. Rather we employ simple models for stressor shapes and work in the framework of linear isotropic elasticity. We account for the screening influence of the free surface on the stressor elastic fields as it was proposed in ref. [36]. In the background section we provide necessary relations on the elasticity of subsurface point stressors and subsurface dilatating ellipsoidal inclusions. We present a survey on the **k·p** approach in calculating the response of the electronic subsystem of the material on the external or internal strain [1]. The background is also devoted

to the consideration of strain-induced polarization in nitride semiconductors. In the main part of the paper we develop the model for buried stressors in uniform GaN and GaN with an embedded quantum well. Then, the results of the model are presented and discussed with emphasis on the lateral change in the energy gap due to strain-induced QD inside the QW in III-nitride binary and ternary compounds.

II. Background

A. *Elasticity of subsurface stressors*

Practically all effects of QDs on the surrounding material depend on their long-range elastic field. From this point of view, an individual QD serves as a *stressor*, *i.e.* a source of elastic strains and stresses. The elastic field of the stressor depends on the geometry of the stressor, *i.e.* its volume and shape as well as the character of intrinsic distortions of the stressor, *e.g.* the crystal lattice mismatch between dot and matrix materials or differences in thermal expansion coefficients. Furthermore the elastic field depends on the elastic properties both inside the stressor material and the surrounding matrix as well as the position of the stressor with respect to interfaces and free surfaces. Independent of quantum dot applications, the mechanical properties of stressors were extensively studied in solid mechanics starting with Eshelby's work on elastic inclusions [37,38].

A complete solution of the elasticity problem in the most general case of stressors in closed analytical form is not possible. For problems related to QDs, three main methods have been applied to determine the elastic behavior of the stressor, namely: (i) theory of elastic inclusions based on exact or approximate analytical solutions of elasticity equations ('Eshelby-like' or related approaches) [11,14,25,27,36]; (ii) finite element methods (FEM) [29,36,39,40]; and (iii) atomistic modeling [41,42]. Approaches *(i)* to *(iii)* all have their particular advantages and disadvantages. FEM is very effective for specific cases but does not provide general solutions and is furthermore affected by choice of boundary conditions for the modeling domain. Atomistic models require accurate interatomic potentials and are further restricted to small systems of atoms in comparison with dot sizes and the surrounding matrix.

The theory of elastic inclusions provides integral expressions for elastic fields which can be expressed in closed analytical form in special cases, *e.g.* relatively simple inclusion shapes in elastically isotropic media. In many cases, it is sufficient to apply such a simplified description. In this paper, we utilize two analytic approaches in stressor mechanics which include the effect of the free surface and the dot shape, *i.e.* a *point stressor* (PS) and a dilatating *ellipsoidal inclusion* (EI), which are shown schematically in Fig. 2.

In the application to semiconductor QDs, stressors originate from the crystal lattice mismatch, which can be described with the help of the misfit parameter

$$f = \frac{a_{\mathrm{m}} - a_{\mathrm{d}}}{a_{\mathrm{d}}} \tag{1}$$

where a_{d} and a_{m} are crystal lattice parameters for dot and matrix materials, respectively. Here, we assume isotropic mismatches, *i.e.* the misfit f is the same in three orthogonal directions. This assumption defines a so-called dilatating stressor, since the dilation (relative change of the volume) inside the stressor is $3f$. Distortions in the surrounding matrix also increase with stressor volume V. Therefore, stressors can be characterized by their strength $S = fV$. Below we will employ the strength S as the main parameter for the dilatating stressor.

The simplest approach to express the far field of dilatating stressors is to ignore their geometry altogether, and to consider them as point sources of dilatation (see Fig. 2a) of given effective strength S, *i.e.* consider them as PSs. The stresses $\sigma_{ij}^{\mathrm{PS}}$ due to a PS can be found by combining the stresses of point force dipoles. Note that if the response of a body to a point force (*i.e.*, the Green's function) is known, the elastic fields caused by any distribution of forces can be obtained by linear superposition [43]. In the case of a PS of expansion, three mutually perpendicular pairs of forces (each pair consists of a dipole of opposing forces of magnitude

P,separated by a distance *d* along their mutual line of action) may be used (see Fig. 2a). Throughout this paper we refer to such a stressor as *positive* PS (*i.e.*, a positive stressor itself would have a larger lattice constant than the surrounding matrix). If one considers a cube of volume $V = d^3$, the average stress in the cube is $\dfrac{P}{d^2}$, which in turn can be related to the strains arising from the misfit *f* via Hooke's law. Based on such considerations one can relate the PS strength to *P* and *d*:

$$S^{PS} = \frac{Pd}{2G}\frac{1-2\nu}{1+\nu}, \tag{2}$$

where *G* is the isotropic material shear modulus and ν is Poisson's ratio. By taking the limit as $d \to 0$, maintaining *Pd* constant, the complete elastic field for a positive PS of expansion with given strength *S* may be determined. The analytic form for the elastic fields of the PS exists in all those cases when the Green's function has a closed solution. The stresses σ_{ij}^{PS} for a PS placed at the distance *h* away from the free surface of an isotropic half-space are given in the Appendix, see Eq. A1. The strain components ε_{ij}^{PS} can be found from stresses by applying Hooke's law, *i.e.* Eq. A4. For example, the important hydrostatic strain component

$\varepsilon_{hydro}^{PS}(r,z) = \varepsilon_{ii}^{PS} = \sum\limits_{i=1}^{3}\varepsilon_{ii}^{PS}$ of the subsurface PS can be obtained with the help of Eq. A5 and it is equal to

$$\varepsilon_{hydro}^{PS}(r,z) = S\frac{(1+\nu)(1-2\nu)}{\pi(1-\nu)}\frac{2(z+h)^2 - r^2}{[r^2+(z+h)^2]^{5/2}}, \tag{3}$$

where the cylindrical coordinates (*r*, *z*) are used (note that *z* is identical to x_3 defined in the Appendix). The plot of $\varepsilon_{hydro}^{PS}(r,z)$ is given in Fig. 3a. Due to the presence of the free surface,

the hydrostatic strain field does *not vanish* for the subsurface PS. This property is in contrast to the case of a PS in an infinite isotropic medium and it has important consequence for strain induced changes in the conduction band (see below).

In the near field, strains and stresses diverge in the PS model; therefore a more accurate approximation is required. To take into account the stressor proximity effects in an analytical treatment, we will consider a dilatating ellipsoidal inclusion (EI), as shown schematically in Fig. 2b. In general, the elastic fields of an arbitrarily shaped dilatating inclusion can be determined by integrating the corresponding elastic fields for a PS, *i.e.* by distributing PSs over the finite volume of the inclusion. In the case of an EI, the stresses $\sigma_{ij}^{EI}(\mathbf{r})$ outside the inclusion can be found by integration of PS stresses over the ellipsoid interior V^{EI}:

$$\sigma_{ij}^{EI}(\mathbf{r}) = \int_{V^{EI}} \frac{1}{V^{PS}} \sigma_{ij}^{PS}(\mathbf{r} - \mathbf{r}')dV'. \tag{4}$$

The results of the evaluation of the Eq. 4 are given in the Appendix. In the examples below we discuss an oblate spheroid (EI with two equal semiaxes $a_1 = a_2 > a_3$) at a depth h from the surface. The strength of such a stressor is given by

$$S^{EI} = \frac{4}{3} f \pi a_1^2 a_3. \tag{5}$$

The expressions for stress and strain in this case (see Eqs. A7 and A4) are more cumbersome than those for the PS. However, a more realistic idealization of the stressor geometry is achieved. Thus, using these expressions we can analyze the near field effects and also consider the influence of the aspect ratio of the stressor.

A comparison of exact analytical solutions is given in Fig. 3 for both the EI and PS placed at the same distance h from the free surface and both with the same effective strength

$S^{EI} = S^{PS} = S$. The dilatation field ε_{kk}^{EI} of the EI (Fig. 3a) agrees extremely well with the corresponding dependence for the PS. In the absence of the free surface, the dilatation outside the EI vanishes as originally shown by Eshelby [37]. The individual components of strain and stresses in the far field also demonstrate a remarkable agreement as seen in the Fig. 3b, where the dependencies of radial stains on z are plotted. In the near field (close to the stressor), there is a quantitative difference between the predictions of the two models. The more realistic EI model shows finite values of strain up to the surface of the ellipsoid. Therefore, we will apply the EI description for the analysis the stressor effects in its close proximity. However in the far field, *i.e.* at the distances $l > l_c \approx V^{1/3}$ (in case of not extremely elongated EI) the simpler PS solutions can be successfully used for a comprehensive analysis of stressor induced variation of electronic properties.

B. Conduction and valence band changes in the presence of strain

Mechanical strains, *i.e.* deviations of the unit cell from its geometry in the unstrained crystal, also modify the band structure of semiconductors. For example, the band gap of a semiconductor increases upon hydrostatic compression [44,45]. Commonly, the effects of strain on the band structure can be described using the Bir-Pikus approach [1], which utilizes the **k·p** perturbation theory formalism in order to determine the deviations of the energy bands from those in the unstrained crystal. The **k·p** perturbation theory formalism is based on Bloch wave solutions of the Schrödinger equation of the form $\psi_{nk}(r) = u_{nk}(\mathbf{r})\exp(i\mathbf{k}\cdot\mathbf{r})$ where n and k are the band index and the electron wave vector, respectively. Substituting these Bloch functions into the Schrödinger equation one can show that the Hamiltonian operator for the unit cell wave functions $u_{nk}(\mathbf{r})$ can be written as the sum of the Hamiltonian operator for $\mathbf{k} = 0$ and a term

proportional to $\mathbf{k \cdot p}$ with $\mathbf{p} = \dfrac{\hbar}{i}\nabla$. Furthermore, the eigenfunctions $u_{n0}(\mathbf{r})$, i.e. for $\mathbf{k} = 0$, form a complete set of eigenfunctions such that all $u_{nk}(\mathbf{r})$ may be written as linear combination of all $u_{n0}(\mathbf{r})$, also known as the *Luttinger-Kohn representation* [1]. Hence, one can apply first-order perturbation theory with a perturbation $\mathbf{k \cdot p}$ and a basis $u_{n0}(\mathbf{r})$ to investigate the band structure in the vicinity of $\mathbf{k} = 0$. The new eigenstates will then be the linear combination of the $u_{n0}(\mathbf{r})$. One common example is the Luttinger-Kohn model, which describes the valence band structure of common III-V semiconductors [2]. Bir and Pikus [1] showed that the form of the strain dependence of the Hamiltonian is essentially identical to the k-dependence of the Hamiltonian. For example, a term proportional to $k_x k_y$ corresponds to a term proportional to the strain component ε_{xy}.

In unstrained wurtzite GaN, there are three closely spaced top valence bands (VBs) at the Brillouin-zone center, usually referred to as heavy-hole (HH), light-hole (LH) and crystal-field split-off hole (SCH) [46,47]. These valence band states have atomic *p*-orbital character in contrast to the bottom conduction band (CB), which has atomic *s*-orbital character. Since the large band gap of GaN reduces the interaction of CB and VB states, the Hamiltonian for the strain dependence of the VB can be separately given by the 6×6 matrix [3]:

$$H^v = \begin{bmatrix} F & 0 & -H* & 0 & K* & 0 \\ 0 & G & \Delta & -H* & 0 & K* \\ -H & \Delta & \lambda & 0 & I* & 0 \\ 0 & -H & 0 & \lambda & \Delta & I* \\ K & 0 & I & \Delta & G & 0 \\ 0 & K & 0 & I & 0 & F \end{bmatrix} \tag{6}$$

with the following strain dependent elements:

$$F = \Delta_1 + \Delta_2 + \lambda + \theta,$$

$$G = \Delta_1 + \Delta_2 + \lambda + \theta,$$

$$H = i(A_6 k_z k_+ + A_7 k_+ + D_6 \varepsilon_{z+}),$$

$$I = i(A_6 k_z k_+ - A_7 k_+ + D_6 \varepsilon_{z+}),$$

$$K = A_5 k_+^2 + D_5 \varepsilon_+,$$

$$\Delta = \sqrt{2} \Delta_3,$$

$$\lambda = A_1 k_z^2 + A_2 k_\perp^2 + D_1 \varepsilon_{zz} + D_2 (\varepsilon_{xx} + \varepsilon_{yy}),$$

$$\theta = A_3 k_z^2 + A_4 k_\perp^2 + D_3 \varepsilon_{zz} + D_4 (\varepsilon_{xx} + \varepsilon_{yy}),$$

$$\varepsilon_+ = \varepsilon_{xx} - \varepsilon_{yy} + 2i\varepsilon_{xy},$$

$$\varepsilon_{z+} = \varepsilon_{xz} + i\varepsilon_{yz},$$

$$k_+ = k_x + ik_y,$$

$$k_\perp^2 = k_x^2 + k_y^2.$$

The parameters D_j ($j = 1$ to 6) are the deformation potentials for the VB, and A_j ($j = 1$ to 7) are equivalent to the Luttinger parameters (see ref. [46] for details) and determine the hole effective masses; ε_{lm} and k_l ($l, m = x, y, z$) are the strain and wavevectors components, respectively. Δ_1 is the crystal-field parameter, while Δ_2 and Δ_3 are the spin-orbit energy parameters. The basis for H^v is given by the usual choice $\frac{1}{\sqrt{2}}|X + iY, \alpha\rangle$, $\frac{1}{\sqrt{2}}|X + iY, \beta\rangle$, $|Z, \alpha\rangle$, $|Z, \beta\rangle$, $\frac{1}{\sqrt{2}}|X - iY, \alpha\rangle$,

$\frac{1}{\sqrt{2}}|X - iY, \beta\rangle$. Here, $|X\rangle$, $|Y\rangle$, and $|Z\rangle$ have the symmetry properties of the atomic p_x, p_y, and p_z orbital functions. $|\alpha\rangle$ and $|\beta\rangle$ denote the spin wavefunctions corresponding to spin up and spin down. The diagonalization of the above matrix yields the three distinct VB maxima $E_{v,j}$.

The Hamiltonian for the strain dependence of the CB minimum is given by a 2×2 matrix with basis $|S, \alpha\rangle$ and $|S, \beta\rangle$. The eigenvalue of the Hamiltonian can be expressed by

$$E_c = \alpha_\parallel \varepsilon_{zz} + \alpha_\perp (\varepsilon_{xx} + \varepsilon_{yy}) + \frac{\hbar^2 k_z^2}{2m_{e\parallel}} + \frac{\hbar^2 k_\perp^2}{2m_{e\perp}}, \tag{7}$$

where $\alpha_\perp$, $\alpha_\parallel$. and $m_{e\parallel}$, $m_{e\perp}$ denote the CB deformation potentials and electron effective mass, respectively. Since in the following analysis we will be only interested in the ground state energies ($\mathbf{k} = 0$), we will find that the above expressions of Eqs. 6 and 7 are substantially simplified.

C. Polarization effects in nitride semiconductors

A sizable red-shift of the ground-level transitions of wurtzite nitride semiconductor quantum wells has been observed by various groups [48,49,50,51] for increasing well width. This phenomenon is sometimes accompanied by the concomitant reduction of the oscillator strength and by the increase of the decay time of the transition. All together, these effects point towards the existence of strong built-in electrostatic fields in wurtzite nitride semiconductors, which causes a substantial quantum-confined Stark effect (QCSE) [3]. The underlying phenomenon is the presence of large electrical polarization fields in wurtzite nitride semiconductors: the spontaneous polarizations are of the same order of magnitude as those of ferroelectrics [52]. As we already mentioned in the Introduction, the magnitude of the piezoelectric constants considerably exceeds that of other III-V semiconductors.

The presence of polarization is strongly connected to the unit cell symmetry of a crystal. Nitride semiconductors exist in both the zincblende and wurtzite structures. In both cases, each group-III atom is tetrahedrally coordinated to four nitrogen atoms. The main difference between these two structures is the stacking sequence of close packed diatomic planes. These stacking sequences are ABABAB along the wurtzite {0001} directions and ABCABC along the zincblende {111} directions. This difference in stacking sequence results in distinct space group symmetries: $P6_3mc$ for wurtzite and $F\bar{4}3m$ for zincblende.

In the absence of external electric fields, the total macroscopic polarization **P** of a solid is the sum of the spontaneous polarization of the equilibrium structure and of the strain-induced, piezoelectric polarization. The zincblende compound semiconductors such as GaAs and InP have four symmetry equivalent polar <111> axes whose contributions cancel each other in equilibrium. Hence, these materials are free of electrical polarization at equilibrium. In contrast, the wurtzite phase has a singular polar axis, namely, the [0001] axis. Thus, the wurtzite phase has a spontaneous electrical polarization parallel to the [0001] direction even at equilibrium.

In practice, semiconductor layers are often grown under strain due to the lattice mismatch with the underlying substrate. Such deformations of the unit cell can lead to additional piezoelectric polarization. The presence of this kind of polarization is again closely related to the unit cell symmetry, namely, the lack of inversion symmetry. The contributions of the four polar axes of zincblende structures cancel each other for growth along a <001> direction. However, growth along one of the polar axes reduces the symmetry and the crystal exhibits piezoelectric polarization. In contrast, the wurtzite structure with its unique polar [0001] axis always carry piezoelectric polarization for any growth direction. The total electric polarization **P** is the sum of spontaneous polarization $\mathbf{P}_{sp}$ and piezoelectric polarization $\mathbf{P}_{pz}$.

In general, the elementary cell of material under consideration can be subjected to an arbitrary strain ε_{ij}. By taking into account the symmetry of the space group P6$_3$mc of wurtzite GaN, the piezoelectric polarization is related to strains as [53]:

$$
\mathbf{P}_{pz} = \begin{pmatrix} 0 & 0 & 0 & 0 & e_{15} & 0 \\ 0 & 0 & 0 & e_{15} & 0 & 0 \\ e_{31} & e_{31} & e_{33} & 0 & 0 & 0 \end{pmatrix} \begin{pmatrix} \varepsilon_{xx} \\ \varepsilon_{yy} \\ \varepsilon_{zz} \\ \varepsilon_{yz} \\ \varepsilon_{xz} \\ \varepsilon_{xy} \end{pmatrix} \tag{8}
$$

with the elements e_{ij} of the piezoelectric tensor in Voigt notation [54].

Any spatial change in total polarization **P** leads to a fixed charge $\rho = -\nabla \cdot \mathbf{P}$. Prime examples are two dimensional electron gases at (Al,Ga)N/GaN interfaces and alternating sheet charge in quantum wells giving rise to the quantum-confined Stark effect [3,55]. In the following analysis we will calculate the distribution of fixed charges induced by subsurface stressors.

III. Description of the Model

In our model, shown schematically in Fig. 4, the dilatation stressor is located at $r = (x^2 + y^2)^{1/2} = 0$ and $z = h$. The material surrounding the stressor is considered either to be a uniform GaN matrix or a GaN/In$_x$Ga$_{1-x}$N/GaN single quantum well (QW) which is grown pseudomorphically between the stressor and the free surface. The designations for the characteristic lengths h, h_{QW}, and l_{QW} are also shown in the Fig. 4. The $z = 0$ plane is taken as the (0001) sample surface and the z-axis points into the sample, hence, the z-axis is parallel to [000$\bar{1}$]. As we already discussed in Section IIA, the elastic properties of a medium are, in general, anisotropic and the stressor may have arbitrary shape and size leading to complex elastic field in close vicinity to the stressor, thus, requiring rather elaborate analytical or finite element (FEM) calculations. To simplify the model and proceed with analytically tractable results, the following approximations were employed: (i) the stressor is taken as either point stressor (PS) or dilatation ellispsoidal inclusion (EI); (ii) the same elastic constants were used for (In,Ga)N and GaN; (iii) isotropic elasticity is used with an effective Poisson's ratio and shear modulus, which are derived from anisotropic elastic constants of GaN (see the Appendix for details). We note that the ellipsoidal inclusion provides a good approximation for the elastic fields of inclusions with more complex shapes [36].

As shown in the Background, the strength of the stressor can be defined via $S = fV$, where V is the stressor volume and f is the crystal lattice mismatch between material of the stressor and surrounding material. The volume of the stressor can be directly estimated from the experimental data of QD structures in III-nitride semiconductors [4,56]. We consider QDs embedded in a GaN matrix with typical dot dimensions of around 20 nm as a lateral size in the basal plane and a height along the z-axis of approximately 2 nm, similar to recently reported

GaN dots in an AlN matrix [56]. For simplicity we prescribe a volume of 200π nm^3 to the stressor. In our numerical examples we will always use this value for V.

The effective misfit parameter f for wurtzite semiconductors can be estimated by taking into account the difference in crystal lattice translations in the basal plane and in the z-axis direction. The lattice parameters of III-nitrides are given in Table II. For such materials one can introduce a pair of misfit parameters, *i.e.* f_a and f_c:

$$f_a = \frac{a_m - a_d}{a_d}; \quad f_c = \frac{c_m - c_d}{c_d}, \tag{9a,b}$$

where a_m, a_d and c_m, c_d are the a and c are the wurtzite lattice parameters of the matrix and the dot, respectively. Then, the effective stressor/matrix mismatch can be defined as

$$f = \frac{2f_a + f_c}{3}. \tag{10}$$

The results of Eq. 10 are summarized in the Table III for a number of possible combinations of the dot and matrix materials. One can see that for III-nitrides both "positive" ($f > 0$) and "negative" ($f < 0$) stressors can be realized (at least hypothetically).

After the strength of the stressor is determined via the effective misfit f and the effective volume V, the elastic field $\varepsilon_{ij}^{stressor}$ induced in the matrix by the stressor is found by applying the formulas for PS and EI described in the Background section. As it follows from the analysis for the case of elastic isotropy, the only material parameter appearing in the stressor strain distributions is Poisson's ratio. Since wurtzite GaN is elastically anisotropic, we choose to use an effective Poisson's ratio $\bar{v}$ (given by Eq. A18 in the Appendix), which was derived by averaging Poisson's ratios along the three mutually perpendicular axes chosen in characteristic crystallographic directions:

$$\bar{v} = -\frac{1}{3}\left(\frac{s_{13}}{s_{33}} + \frac{s_{12} + s_{13}}{s_{11}}\right). \tag{11}$$

where s_{ij} are the elastic compliances for GaN. Using the elastic constants from ref. [57] we

obtain $\bar{v} = 0.234$.

When a pseudomorphically grown single QW is considered, additional uniform strains

ε_{ij}^{QW} are generated inside the well:

$$\varepsilon_{xx}^{QW} = \varepsilon_{yy}^{QW} = f_{QW}; \quad \varepsilon_{zz}^{QW} = -\frac{2\bar{v}}{1-\bar{v}} f_{QW}. \tag{12a,b}$$

where the misfit parameter for the QW f_{QW} is defined as

$$f_{QW} = \frac{a_m - a_{QW}}{a_{QW}}. \tag{13}$$

The in-plane lattice parameter a_{QW} of the QW material with the composition $In_xGa_{1-x}N$ can be

found in accordance with the Vegard's law:

$$a_{QW} = xa_{InN} + (1-x)a_{GaN}. \tag{14}$$

Using Eqs. 13 and 14 and taking into account the data for the lattice parameters of GaN and InN

(Table II), we obtain f_{QW} = -0.016 and -0.0055 for In contents of x = 0.15 and 0.05,

respectively.

Finally, the combined action of the stressor and the QW is given by the superposition of

the corresponding elastic strains:

$$\varepsilon_{ij}^{total} = \varepsilon_{ij}^{stressor} + \varepsilon_{ij}^{QW}. \tag{15}$$

To evaluate the influence of the stressor on the material electronic properties we apply a **k·p**

approach as presented in the Background. For deformation potentials of GaN we use the Set I

from the Table IV that corresponds to parameters utilized in our preliminary publication [26]. Because the data on deformation potentials for wurtzite III-nitrides are diverse, we also have checked different sets of values, which are also included as Set II and Set III in the Table IV. Set II are recommended band structure parameters from a recent review article by Vurgaftman and Meyer [58] and Set III represents the data used by Van de Walle in his study of "absolute" deformation potentials and the band offsets at wurtzite III-nitrides heterojunctions [59]. We note that in spite of distinctly different values of the individual deformation potentials, all three sets provide comparable values for interband deformation potentials, $i.e.$, $a_1 = \alpha_{\parallel} - D_1$ and $a_2 = \alpha_{\perp} - D_2$. It also will be shown in the next section that all the above sets of parameters have the similar effect on the band edge shifts in III-nitrides induced by subsurface stressors.

For the analysis of the stressor induced polarization charges we use the following values of piezoelectric coefficient for GaN: $e_{33} = 0.73$ Cm^{-2}, $e_{31} = -0.49$ Cm^{-2} [60], and $e_{15} = -0.40$ Cm^{-2}, where the value of the coefficient e_{15} is the estimate obtained on the averaging the data reported in refs. [25] and [61].

IV. Stressor-Induced Band Edge Shifts

The change of the valence band structure is *non-linear* with strain as these energies represent the eigenvalues of a 6×6 Hamiltonian in the **k·p** calculations, see the Background section for details. We will examine the shifts of the conduction and valence band edges due to the subsurface stressor strain field by utilizing the **k·p** perturbation approach developed by Bir and Pikus [1] and employing the corresponding deformation potentials for GaN [3]. Due to strain, both the CB and the VB states, *i.e.* heavy-hole (HH), light-hole (LH) and crystal-field split-off hole (SCH), are modified leading to shifts of the corresponding band edges relative to their values for unstrained material. The stressor strain field leads to changes in the original VB states such that it is no longer correct to simply describe them as HH, LH and SCH [26]. Therefore we label the individual VBs as top, middle and bottom VB according to their energy with the top VB being closest to the CB.

The shifts of the CB energies E_c^{def} in a uniform GaN matrix due to positive and negative subsurface PSs are shown in Fig. 5. We use parameters for the PSs that are equivalent in the far field to $In_{0.5}Ga_{0.5}N$ and AlN QDs with misfit parameters $f = 0.051$ and $f = -0.030$, respectively. All the results shown for the PS are calculated within the valid range of the point source approximation as we do not approach the point source closer than its characteristic length l_c. The shift of the CB is proportional to the hydrostatic strain (*e.g.* see Eq. (7) in background section), hence, Fig. 5 resembles Fig. 3a in different units. We see that either a positive or negative PS leads to only slight changes in the CB energy in the subsurface region above the stressor. In contrast, the changes in the VB energies E_v^{def} (induced by PSs and shown in Fig. 6) show a rather complex dependence on the actual location. In-plane and out-of-plane cross-sections of the VB structure are shown along the z-axis and for two different depths z in Fig. 6a, and Figs. 6b

and c, respectively. In Figure 6 the left column gives results for the positive PS, whereas the right column provides the results for the negative PS. The lower part of the figure, *i.e.* Fig. 6d, presents results for the other set of band structure parameters, namely Set II from Table IV. Near the surface the VBs have relative separations only slightly different from the values of unstrained material, see Fig. 6a. However, in the case of the positive PS, with increasing depth z, the separation of the top and middle VBs decreases until they cross (at $z \approx 25$ nm for the parameters used for Fig. 6). Finally, the top VB moves towards the CB while the other two VBs bend away from the CB, maintaining their separation. For the negative PS such a behavior is not observed, in this case no crossing occurs but both the top and the middle VBs move towards the CB when approaching the negative PS.

As it follows from Figs. 6b and 6c (left and right), for $r > h$, the VBs are only weakly affected by the presence of the stressor regardless of the depth z. Close to the sample surface (Fig. 6b), the relative positions of the VBs only change slightly close to the symmetry axis. This influence is due to hydrostatic component of the strain tensor. When approaching the stressor, see Fig. 6c, its effect becomes visible even still inside the region of the far field approximation. The remarkable feature of the PS influence on the VB structure is the unidirectional effect of positive and negative stressors. Both types of stressor raise the top VB level.

It is clear from the comparison of the Figs. 6c and 6d that the use of the different set of deformation potential parameters, *i.e.* Set II instead Set I, does not change the main conclusion on the character of the stressor influence on the shift of the valence band edge. The same observation was also obtained for the parameters of Set III from the Table IV. Therefore all the following reported results were obtained by using the deformation potential parameters of Set I.

It is interesting to consider the case of a GaN/In$_x$Ga$_{1-x}$N/GaN QW structure which will provide vertical confinement of the carriers. The total strain field from Eq. 15 was used as input for the Hamiltonian in the **k·p** calculations. For a positive stressor we obtained a CB potential exhibiting lateral electron confinement at $r = 0$ regardless of the actual depth of the quantum well. However, holes will be either trapped away or at $r = 0$ depending on the actual location of the well. Therefore, we identify two important possibilities. For a shallow well close to the surface, electrons and holes show significant lateral separation and thus would have low radiative recombination rates. However, for a quantum well sufficiently close to the stressor, both electrons and holes may be trapped at $r = 0$ in such a way that they are spatially localized resulting in a strain-induced quantum dot inside the quantum well. To investigate this effect in detail we use an EI instead of a PS since the QW may stay in close proximity to a stressor.

Figure 7 provides the results of the VB calculations for an EI placed at the depth $h = 41$ nm in a GaN matrix with an additional QW characterized by $h_{QW} = 3$ nm, and $l_{QW} = 4$ nm. The material for the EI was chosen to be either In$_{0.5}$Ga$_{0.5}$N (positive stressor with $f = 0.051$) or AlN (negative stressor with $f = -0.030$); the volume of the EI was taken as $V = 200\pi$ nm^3. The material in the In$_x$Ga$_{1-x}$N QW corresponds to either x = 0.05 (moderate strained well) or x = 0.15 (strongly strained well). From the analysis of the plots we may see the difference regarding the results obtained for the point stressor. In the case of positive EI, the local minimum in the VB profile emerges just above the center of the ellipsoid, *i.e.* at $r = 0$. For a strongly strained QW the minimum can be even lower than the far field (large r) VB energy level, as shown in Fig. 7b. At the same time, there is a pronounced maximum of the order of 50 to 100 meV shifted towards the ends of ellipsoid. For a negative EI, the top VB has the maximum above the inclusion center.

The characteristic change in E_v^{def} with respect to the values for the QW in the absence of the stressor is ~50 meV.

In the general case, from our simplified description we cannot predict the exact positions of VB and CB edges but can provide only relative change in their energy due to deformation effects. Useful information, however, can be obtained for the change of the energy gap ΔE_g in strain-induced QD, as it is presented in Fig. 8. In the z-direction there is a sharp change of ΔE_g, which is caused mainly by the chemical composition and uniform strain inside the QW. This effect is combined with the effect of the stressor. In the r-direction the influence of the non-uniform strain of the EI manifests itself more clearly. For example, the negative stressor (see Fig. 8b right) demonstrates the non-uniform strain-related reduction of the band gap of the order of 50 meV. To calibrate the results of the calculations we utilized the following value for the gap change in the strained $In_{0.15}Ga_{0.85}N$ QW: ΔE_g^{QW} = -0.61 eV. This value was obtained by extrapolating the experimentally found coefficient $\dfrac{dE_g}{dx}$ = -4.1 eV for pseudomorphically strained $In_xGa_{1-x}N$ layers [62]. It is clear from Fig. 8b that negative stressors in the vicinity of QWs can give rise to strain-induced dots within the wells.

V. Stressor-Induced Polarization Charges

The density of fixed polarization charges in the system with the stressor is related to local variations of the total polarization $\mathbf{P}$, which is the sum of the spontaneous and the piezoelectric polarization $\mathbf{P}_{sp}$ and $\mathbf{P}_{pz}$, respectively. The spontaneous and piezoelectric polarization constants of ternary alloys are linearly interpolated between the corresponding values of the binaries. For calculating $\mathbf{P}_{pz}$ we employ (see Eq. 8 above) the piezoelectric tensor of wurtzite nitride semiconductors, which gives us

$$\mathbf{P}_{pz} = \begin{pmatrix} e_{15}\varepsilon_{xz} \\ e_{15}\varepsilon_{yz} \\ e_{31}(\varepsilon_{xx} + \varepsilon_{yy}) + e_{33}\varepsilon_{zz} \end{pmatrix}, \tag{16}$$

where the piezoelectric constants of GaN e_{31}, e_{33} and e_{15} has the values given in the section III. Finally, the density of fixed polarization charges $\rho(x, y, z)$ is given by $-\nabla \cdot \mathbf{P}$.

The example of these calculations is shown in Fig. 9 for the positive stressor in the absence of a quantum well. The fixed charge density ρ exhibits the same symmetry as the strain field, i.e. rotational symmetry with respect to the z-axis, *i.e.* $\rho(x, y, z) = \rho(r, z)$. This finding is due to the symmetry of the piezoelectric tensor and it is in contrast to the case of a stressor in a zincblende crystal where the z-axis has $\overline{4}$ symmetry axis for the polarization charge density leading to a quadrupole of the fixed electric charge density [14]. As seen from Fig. 9, both positive and negative polarization charges are present. For large in-plane separations r, we have a relatively low density of negative fixed charges in the 10^{16} cm^{-3} range. As we approach the z-axis, we can distinguish two regimes. Close to the surface, we have positive fixed charges in the mid to high 10^{16} cm^{-3} range. This charge density can be easily screened by free electrons taking into account the usually reported unintentional n-type doping level of 10^{16}-10^{17} cm^{-3} in

GaN. In contrast, for larger depths negative fixed charges are found which can be as high as in the mid 10^{18} cm^{-3} range at a distance of l_c from the stressor on the z-axis.

In general, one has to combine the effects of deformation potentials and polarization charges in order to obtain self-consistent solutions for wave functions and energies of electrons and holes. Therefore, one has to solve both the Schrödinger and the Poisson equations simultaneously which is straightforward in one-dimension (see *e.g.*, ref. [63]), however, is a substantial numerical task in two or three dimensions. In this work we restricted ourselves to the uncoupled effects of deformation potentials and polarization charges but will pursue self-consistent solutions in future work.

In the absence of solutions of both the Schrödinger and the Poisson equations, we can still gain insight into the results of this work. In n-type material, the Fermi level should remain close to the CB, thus most, if not all, of the strain-induced band motion will be in the VB. A positive stressor will give rise to a negative polarization-induced fixed charge density in the surrounding matrix (see Fig. 9) and additionally, a positive stressor in n-type material will cause upward motion of the VB (see Fig. 6). Thus, in n-type materials, excess holes, such as generated by photoexcitation or electrical injection, will be attracted to the stressor. $In_xGa_{1-x}N$ or InN dots in an n-type GaN matrix should be a reasonable realization of this case – the $In_xGa_{1-x}N$ dots will be a positive stressor and intentional or unintentional doping of the GaN matrix is readily achieved. Analogous arguments can be developed for negative stressors. In this case, favorable structures p-type matrices with negative stressors would attract minority carriers (electrons in this case).

VI. Summary and Conclusions

We have investigated the influence of non-uniform elastic field that originates from a subsurface stressor (e.g., quantum dot) on the electronic properties of III-nitrides. Two different analytical models of subsurface stressors were explored: (i) point source of dilatation, *i.e.* point stressor (PS) and (ii) dilatation ellipsoidal inclusion (EI). The stressor effective strength was shown to be equal to the product of the inclusion volume V and lattice mismatch f between the materials of the inclusion and surrounding matrix. The cases of "positive" (*e.g.*, $In_{0.5}Ga_{0.5}N$ inclusion, $f = 0.051$) and "negative" (*e.g.*, AlN inclusion, $f = -0.030$) stressors in GaN matrix have been considered. It was argued that the PS model is valid for all stressors in the far field and therefore can be applied with a good accuracy at distance $l > l_c \approx V^{1/3}$ (in case of not extremely elongated inclusions).

We proposed and analyzed the following material structure design: a uniform semi-infinite GaN matrix with a buried stressor or GaN matrix with a single $In_xGa_{1-x}N$ ($x = 0.05$ and 0.15) quantum well which is grown pseuodomorphically between the stressor and the free surface. The presence of the strained QW is responsible for the vertical confinement for electron and holes, whereas the presence of the buried stressor can provide lateral confinement of the carriers.

To examine the shifts of the conduction and valence band edges caused by the stressor we applied a **k·p** perturbation theory approach with prescribed values of deformation potentials typical for III-nitrides. We found that buried stressors only affect the conduction band in the near surface region. For "deep" stressors (placed at large distance) from the surface the effect is small. Significant influence has been found of stressors on the valence band shift. It has been demonstrated that both negative and positive stressors cause upward motion of top valence band.

In the vicinity of the either an AlN or $In_{0.5}Ga_{0.5}N$ stressor, the change in energy of the top valence band can be on the order of 50 meV. Stressors in the vicinity of a quantum well provide the possibility for forming strain-induced quantum dots within the quantum well with lateral confinement also on the order of 50 meV.

In addition to the effect of band edge shift and the change in the energy gap via deformation potentials, subsurface stressors are responsible for the formation of polarization charges, with their distribution depending on symmetry of the piezoelectric tensor and the character of the stressor deformation field. It was shown that positive stressors with strength typical for experimentally observed in III-nitrides quantum dots give rise to large negative space charge in the vicinity of the stressor.

A complete understanding of the optical emission behavior of III-N structures should include effects of heterogeneous strain caused by composition fluctuations, dislocations, and intentional or unintentional stressors.

Acknowledgements

Appendix

Stresses for the point source of dilatation – "positive" PS

In the coordinate system (x_1, x_2, x_3) related to the free surface of the isotropic half space,

the PS occupies the position $(0,0,h)$. Its stresses are [36,64]:

$$\sigma_{ij} = S \frac{G(1+v)}{2\pi(1-v)} \left[\frac{\partial^2}{\partial x_i \partial x_j} \left(-\frac{1}{R_1} \right) + v\delta_{ij} \frac{\partial^2}{\partial x_3^2} \left(\frac{4}{R_2} \right) - x_3 \frac{\partial^3}{\partial x_3 \partial x_i \partial x_j} \left(\frac{2}{R_2} \right) \right.$$

$$\left. + (-4v+3)(-1+\delta_{3i}+\delta_{3j}) \frac{\partial^2}{\partial x_i \partial x_j} \left(\frac{1}{R_2} \right) - \delta_{3j} \frac{\partial^2}{\partial x_3 \partial x_i} \left(\frac{1}{R_2} \right) - \delta_{3i} \frac{\partial^2}{\partial x_3 \partial x_j} \left(\frac{1}{R_2} \right) \right],$$

(A1)

where S is the PS strength, G is the shear modulus, v is Poisson's ratio, δ_{ij} is Kroneker delta,

and $R_{1,2} = \sqrt{x_1^2 + x_2^2 + (x_3 \mp h)^2}$. The hydrostatic pressure is defined as

$$p = -\frac{1}{3}\sigma_{kk} = -\frac{1}{3}\sum_{k=1}^{3}\sigma_{kk},$$

(A2)

which gives the following result for the subsurface PS:

$$p = -\frac{2S}{3}\frac{G(1+v)^2}{\pi(1-v)}\frac{\partial^2}{\partial x_3^2}\left(\frac{1}{R_2}\right).$$

(A3)

Strains are related to the stresses via the Hooke's law:

$$\varepsilon_{ij} = \frac{1}{2\mu}\left(\sigma_{ij} - \frac{v}{1+v}\sigma_{kk}\delta_{ij}\right).$$

(A4)

Local dilatation (hydrostatic strain) is expressed as

$$\varepsilon_{\text{hydro}} = \varepsilon_{ii} = \sum_{i=1}^{3}\varepsilon_{ii} - \frac{3}{2\mu}\frac{1-2v}{1+v}p,$$

(A5)

where the coefficient in front of the pressure p on the right hand side of Eq. A5 has the meaning

of inverse bulk modulus.

Stresses for the dilatating ellipsoidal inclusion – "positive" EI

As shown by Mura [43,64], the stress field for an EI in a half-space can be obtained by integrating the displacement field that gave rise to Eq. (A1) over the domain

$$\frac{x_1'^2}{a_1^2} + \frac{x_2'^2}{a_2^2} + \frac{(x_3'-h)^2}{a_3^2} \le 1, \tag{A6}$$

where a_1, a_2, and a_3 denote the semi-axes of the ellipsoid along the respective coordinate directions, and h denotes the depth of the center of the ellipsoid from the surface. For points exterior to the inclusion, the stress components take the form

$$\sigma_{ij} = S \frac{G(1+v)}{2\pi(1-v)} \left[-\frac{\partial^2 \psi}{\partial x_i \partial x_j} - x_3 \frac{\partial^3 \varphi}{\partial x_3 \partial x_i \partial x_j} + 4v \, \delta_{ij} \frac{\partial^3 \varphi}{\partial x_3^2} \right.$$
$$\left. - (3-4v)(\delta_{3i} + \delta_{3j} - 1)\frac{\partial^3 \varphi}{\partial x_i \partial x_j} - (\delta_{3i} + \delta_{3j})\frac{\partial^3 \varphi}{\partial x_i \partial x_j} \right], \tag{A7}$$

where

$$\psi = \frac{3}{4} \int_\lambda^\infty \frac{1 - \left(\dfrac{y_1^2}{a_1^2 + s} + \dfrac{y_2^2}{a_2^2 + s} + \dfrac{y_3^2}{a_3^2 + s} \right)}{\sqrt{(a_1^2 + s)(a_2^2 + s)(a_3^2 + s)}} \, ds \tag{A8}$$

with

$$\frac{y_1^2}{a_1^2 + \lambda} + \frac{y_2^2}{a_2^2 + \lambda} + \frac{y_3^2}{a_3^2 + \lambda} = 1; \tag{A9}$$

and

$$\varphi = \frac{3}{4} \int_\mu^\infty \frac{1 - \left(\dfrac{z_1^2}{a_1^2 + s} + \dfrac{z_2^2}{a_2^2 + s} + \dfrac{z_3^2}{a_3^2 + s} \right)}{\sqrt{(a_1^2 + s)(a_2^2 + s)(a_3^2 + s)}} \, ds \tag{A10}$$

with

$$\frac{z_1^2}{a_1^2 + \mu} + \frac{z_2^2}{a_2^2 + \mu} + \frac{z_3^2}{a_3^2 + \mu} = 1. \tag{A11}$$

The coordinate transformation for y_i and z_i is defined such that

$$y_1 = z_1 = x_1, \qquad y_2 = z_2 = x_2, \qquad y_3 + h = z_3 - h = x_3. \tag{A12}$$

It was found that the integrals represented by Eqs. A8 and A10, which require the roots of Eqs. A9 and A11, respectively, for λ and μ, can be obtained analytically in terms of elementary functions if at least two of the semi-axes a_1, a_2, and a_3 are equal [36]. We make use this property in our analysis of subsurface EI influence on the materials band structure.

Effective Poisson's ratio in materials with wurtzite crystal structure

Poisson's ratio ν of a material is defined as $\nu = -\dfrac{\varepsilon_{trans}}{\varepsilon_{long}}$ where ε_{long} and ε_{trans} are the longitudinal and the transverse strain responses, respectively, to a longitudinal tensile stress (load) σ_{long}. It is assumed that the transverse direction is stress-free.

Wurtzite GaN is elastically anisotropic, hence, the Poisson's ratio is also anisotropic. Here, we choose to use an isotropic Poisson ratio $\bar{\nu}$ which is obtained by averaging the three Poisson ratios along the three Cartesian axes, which correspond to high symmetry directions of wurtzite. These individual Poisson's ratios are obtained using the Hooke's law relation between normal stresses and strains in a case of elastic anisotropy:

$$\begin{pmatrix} \varepsilon_{xx} \\ \varepsilon_{yy} \\ \varepsilon_{zz} \end{pmatrix} = \begin{pmatrix} s_{11} & s_{12} & s_{13} \\ s_{12} & s_{11} & s_{13} \\ s_{13} & s_{13} & s_{13} \end{pmatrix} \begin{pmatrix} \sigma_{xx} \\ \sigma_{yy} \\ \sigma_{zz} \end{pmatrix} \tag{A13}$$

where s_{ij} are the elastic compliance constants in Voigt notation [54].

In the following, we express the Poisson ratio $v_{x(y,z)}$ in terms of the stiffness constants by setting $\sigma_{xx(yy,zz)} = \sigma_{long}$ and the two remaining stresses to zero as the transverse directions are free surfaces. Since the xy-plane is chosen normal to the c-direction it is elastically isotropic. Thus the transverse strain is also isotropic in this plane for a given longitudinal strain along the z-axis. Thus, for $\sigma_{zz} = \sigma_{long}$ we obtain

$$s_{13} \times \sigma_{long} = \varepsilon_{xx} = \varepsilon_{yy}, \quad s_{33} \times \sigma_{long} = \varepsilon_{zz} \tag{A14}$$

leading to

$$v_z = -\frac{s_{13}}{s_{33}}. \tag{A15}$$

However, the xz and yz planes are anisotropic. Then for $\sigma_{xx(yy)} = \sigma_{long}$ we get

$$s_{11} \times \sigma_{long} = \varepsilon_{xx(yy)}, \quad s_{12} \times \sigma_{long} = \varepsilon_{yy(xx)}, \quad s_{13} \times \sigma_{long} = \varepsilon_{zz}. \tag{A16}$$

We define an average Poisson's ratio along x (and y) by

$$v_x = v_y = -\frac{s_{12} + s_{13}}{2 s_{11}}. \tag{A17}$$

Finally, we obtain

$$\bar{v} = \frac{2 v_x + v_z}{3} = -\frac{1}{3}\left(\frac{s_{13}}{s_{33}} + \frac{s_{12} + s_{13}}{s_{11}} \right). \tag{A18}$$

Figure Captions

Figure 1   Strain induced quantum dots in semiconductor structures.

(a) QD induced in a QW by a surface stressor, *e.g.* InP or InAs, in materials with zinc blende crystal structure.

(b)   QD induced by buried stressor, *e.g.* InN, in materials with wurtzite crystal structure.

Figure 2   The models proposed for analytical treatment of subsurface stressors in GaN.

(a) Schematic for a point stressor (PS) placed in a GaN layer. The PS is described by three orthogonal force dipoles with separation d and magnitude P acting on the faces of a cube with volume d^3 in the limit of $d \rightarrow 0$.

(b)   Dilatating oblate ellipsoidal inclusion (EI) with volume $V = \frac{4}{3}\pi a_1^2 a_3$ and mismatch f with respect to the surrounding material. Two of three principle diameters of the ellipsoid are assumed to be equal, *i.e.* $a_2 = a_1$.

Figure 3   Comparison of point versus ellipsoidal stressor.

(a) Hydrostatic strain (dilatation field) $\varepsilon_{ii}(r,z)$ induced by the subsurface stressors. The strain is given in units of $\dfrac{S}{\pi h^3}\dfrac{(1+v)(1-2v)}{(1-v)}$, where S is the effective strength of

the stressor placed at the distance h from the free surface of an isotropic half-space and v is Poisson's ratio.

(b) Dependence of the radial strain $\varepsilon_{rr}(0, z)$ on depth in the GaN layer. The stressor (EI or PS) is located at a distance $h = 41$ nm from the surface and has effective strength $S = fV$ equivalent to an $In_{0.5}Ga_{0.5}N$ inclusion with a volume of 200π nm^3 and $f = 0.051$. The strain is normalized by 1.26×10^{-4}, which corresponds to an effective Poisson ratio $\bar{v} = 0.234$ for GaN. Results for ellipsoidal and point stressors are shown by solid and dashed lines, respectively.

Figure 4 Characteristic distances for a buried stressor in GaN layer with embedded QW.

The sample surface $z = 0$ corresponds to the (0001) GaN growth plane with the z-axis in the $[000\bar{1}]$ crystallographic direction.

Figure 5 Map for GaN conduction band edge changes E_c^{def} due to strain fields of buried stressors.

(a) For the positive PS with effective strength $S = fV$ equivalent to an $In_{0.5}Ga_{0.5}N$ inclusion with a volume of 200π nm^3 and $f = 0.051$.

(b) For the negative PS with effective strength $S = fV$ equivalent to an AlN inclusion with a volume of 200π nm^3 and $f = -0.030$. The stressors are located at a distance $h = 41$ nm from the surface The effective Poisson's ratio was taken as $\bar{v} = 0.234$, the contour values are given in meV.

Figure 6 Strain induced change E_v^{def} in the valence band structure of GaN due to the presence of the subsurface point stressors.

(a) Dependence of the valence band maxima on depth z for $r = 0$.

(b), (c), (d) Radial dependencies for the energy of valence bands for $z = 15$, $z = 33$ nm, and $z = 33$ nm (Set II), respectively.

Results for parts (a), (b), and (c) were obtained for deformation potential parameters from the Set I, results for (d) were obtained for deformation potential parameters from the Set II. Valence bands are designated as top, middle and bottom ones, respectively (top closest to the conduction band). The left column presents the results for "positive" PS, with the effective strength S equivalent to $In_{0.5}Ga_{0.5}N$ inclusion with a volume of 200π nm^3 and $f = 0.051$. The right column presents the results for "negative" PS, with the effective strength S equivalent to AlN inclusion with a volume of 200π nm^3 and $f = -0.030$. The distance from the stressor to the layer surface is $h = 41$ nm. The effective Poisson's ratio was taken as $\bar{v} = 0.234$.

Figure 7 Dependence of the strain-induced change E_v^{def} in the valence band structure on spatial coordinates for $GaN/In_xGa_{1-x}N/GaN$ QW sandwich structure in the presence of the subsurface ellipsoidal stressors:

(a) for x = 0.05 and "positive" $In_{0.5}Ga_{0.5}N$ EI;

(b) for x = 0.15 and "positive" $In_{0.5}Ga_{0.5}N$ EI; (c) for x = 0.15 and "negative" AlN EI.

Stressors parameters: volume $V = 200\pi$ nm^3, aspect ratio $a_2 = a_3 = 3$, $h = 41$ nm. QW parameters: $h_{QW} = 3$ nm, $l_{QW} = 4$ nm. The effective Poisson's ratio was taken as $\bar{v} = 0.234$. The dashed lines show the top VB level in the absence of stressor. The plots are given for the bottom of the QW as shown schematically in insert in (b).

Figure 8 Change of the band gap in $GaN/In_xGa_{1-x}N/GaN$ QW sandwich due to buried ellipsoidal stressors.

(a) Band gap dependence on depth z for $r = 0$,

(b) Band gap dependence on the in-plane position near the top and the bottom of the QW.

The left and right columns present results for "positive" $In_{0.5}Ga_{0.5}N$ and "negative" AlN EIs, respectively. Stressors parameters: volume $V = 200\pi$ nm^3, aspect ratio $a_2 = a_3 = 3$, $h = 41$ nm. QW parameters: x = 0.15, $h_{QW} = 3$ nm, $l_{QW} = 4$ nm. The effective Poisson's ratio was taken as $\bar{v} = 0.234$. Dashed line shows the top VB level in the absence of stressor.

Figure 9 Spatial dependence of the subsurface stressor induced fixed polarization charge density.

(a) Map for charge distribution in GaN due to the strain field of the buried stressor; the contour values for the charge density are given in $10^{16}|e|/cm^3$.

(b) Radial dependencies for the charge density for $z = 1$ and $z = 15$ nm, respectively.

The plots were obtained for a "positive" PS located at a distance $h = 41$ nm from the surface and with effective strength $S = fV$ equivalent to an $In_{0.5}Ga_{0.5}N$ inclusion with a volume of 200π nm^3 and $f = 0.0507$. The effective Poisson's ratio was taken as $\bar{v} = 0.234$, the values for polarization coefficients are given in the text.

Table I Comparison of GaAs and GaN response to elastic strain.

Data for GaAs are taken from ref. [14]; for GaN data see section 3.

Material	Band gap (eV)	Interband hydrostatic deformation potential (eV)	Typical magnitude for piezoelectric coefficient (Cm^{-2})
GaAs	1.42	$a_c - a_v = -7.9$	$e_{14} = -0.16$
GaN	3.45	$a_1 = \alpha_{\parallel} - D_1 = -3.1$ $a_2 = \alpha_{\perp} - D_2 = -11.2$	$e_{31} = -0.49$

Table II Crystal lattice parameters of III-nitrides with wurtzite structure [65,58].

Lattice parameters	AlN	GaN	InN
a (Å)	3.112	3.189	3.54
c (Å)	4.982	5.185	5.705

Table III Effective lattice mismatch for wurtzite III-nitrides.

Material		Misfit parameter f
Stressor	Matrix	
GaN	AlN	0.029
InN	GaN	0.096
$In_{0.5}Ga_{0.5}N$	GaN	0.051
AlN	GaN	-0.030

Table IV Band structure parameters of wurtzite GaN.

Parameters	Set I, ref. [3] (eV)	Set II, ref. [58] (eV)	Set III, ref.[59] (eV)
Δ_1	0.022	0.010	-
Δ_2	0.005	0.017	-
$\alpha_{\parallel}$	-45.5	-8.6	-6.0
$\alpha_{\perp}$	-44.5	-6.8	-6.0
D_1	-41.4	-3.7	0.11
D_2	-33.3	4.5	5.54
D_3	8.2	8.2	5.76
D_4	-4.1	-4.1	-3.04
D_5	-4.7	-4.0	-
D_6	$D_6 = (D_3 + 4 D_5)/\sqrt{2}$ (see ref. [46] and references therein).		

References

1. G.L. Bir and G.E. Pikus, *Symmetry and Strain Induced Effects in Semiconductors* (Wiley, New York, 1974).

2. J. Singh, *Electronic and Optoelectronic Properties of Semiconductor Structures* (Cambridge University Press, 2003).

3. S. Ghosh, P. Waltereit, O. Brandt, H.T. Grahn, and K.H. Ploog, Phys. Rev. B **65**, 075202 (2002).

4. K. Hoshino, S. Kako, Y. Arakawa, Phys. Stat. Sol. (b) **240**, 322 (2003).

5. H.K. Cho, J.Y. Lee, J.H. Song, P.M. Yu, S.M. Yang, and C.S. Kim, J. Appl. Phys. **91**, 1104 (2002).

6. D. Leonard, K. Pond, and P.M. Petroff, Phys. Rev. B **50**, 11687 (1994).

7. D. Bimberg, M. Grubdmann, and N.N. Ledentsov, MRS Bulletin **23** (2), 31 (1998).

8. R.J. Warburton, Contemp. Phys. **43**, 351 (2002).

9. S. Kret, T. Benabbas, C. Delamarre, Y. Androussi, A. Dubon, J.Y. Laval, and A. Lefebvre, J. Appl. Phys. **86**, 1988 (1999).

10. A.D. Andreev, J.R. Downes, D.A. Faux, and E.P. O'Reilly, J. Appl. Phys. **86**, 297 (1999).

11. M. Grundmann, O. Stier, and D. Bimberg, Phys. Rev. B **52**, 11969 (1995).

12. H. Jiang and J. Singh, Physica E **2**, 614 (1998).

13. N. Usami, T. Ichitsubo, T. Ujihara, T. Takahashi, K. Fujiwara, G. Sazaki, and K. Nakajima, J. Appl. Phys. **94**, 916 (2003).

14. J.H. Davies, J. Appl. Phys. **84,** 1358 (1998).

15. K.Kash, J.M. Worlock, M.D. Sturge, P. Grabbe, J.P. Harbison, A. Scherer, and P.S.D. Lin, Appl. Phys. Lett. **53**, 782 (1988).

16. K. Kash, R. Bhat, D.D. Mahoney, P.S.D. Lin , A. Scherer,, J.M. Worlock, B.P. Van der Gaag, M. Koza, and P. Grabbe, Appl. Phys. Lett. **55**, 681 (1989).

17. G.W. Bryant, J. Luminesc. **70**, 108 (1996).

18. J. Tulkki and A. Heinämäki, Phys. Rev. B **52**, 8239 (1995).

19. H. Lipsanen, M. Sopanen, and J. Ahopelto, Phys. Rev. B **51**, 13868 (1995).

20. J.H. Davies, Appl. Phys. Lett. **75**, 4142 (1999).

21. W.V. Schoenfeldt, C. Metzner, E. Letts, and P.M. Petroff, Phys. Rev. B **63**, 205319 (2001).

24. J.H. Davies, D.E. Petticrew, and A.R. Long, Phys. Rev. B **58**, 10789 (1998).

25. A.D. Andreev and E. P. O'Reilly, Phys. Rev. B **62**, 15851 (2000).

26. P. Waltereit, A.E. Romanov, and J.S. Speck, Appl. Phys. Lett. **81**, 4754 (2002).

31. G.S. Pearson and D.A. Faux, J. Appl. Phys. **88**, 730 (2000).

32. E. Pan and B. Yang, J. Appl. Phys. **90**, 1487 (2001).

33. Q.X. Pei, C. Lu, Y.Y. Wang, J. Appl. Phys. **93**, 1487 (2003).

34. M.A. Makeev and A. Madhukar, Phys. Rev. B **67**, 073201 (2003).

35. E. Pan and B. Yang, J.Appl. Phys. **93**, 2435 (2003).

36. A.E. Romanov, G.E. Beltz, W.T. Fisher, P.M. Petroff, and J.S. Speck, J. Appl. Phys. **89**, 4523 (2001).

37. J.D. Eshelby, Proc. R. Soc. London, Ser. A **241**, 376 (1957).

38. J.D. Eshelby, Proc. R. Soc. London, Ser. A **252**, 561 (1959).

39. T. Benabbas, Y. Androussi, and A. Levebre, J.Appl. Phys. **86**, 1945 (1999).

40. G. Maralidharan, Jpn. J. Appl. Phys.(Part 2) **39**, L658 (2000).

41. X. Su, R.K. Kalia, A. Nakano, P. Vashista, Appl. Phys. Lett. **79**, 4577 (2001).

42. M.A. Makeev and A. Madhukar, Appl. Phys. Lett. **81**, 3789 (2002).

43.	T. Mura, *Micromechanics of Defects in solids* (Martinus Nijhoff, Boston, 1987).

44.	M. Tchounkeu, O. Briot, B. Gil, J.P. Alexis, and R.-L. Aulombard, J. Appl. Phys. **80**, 5352 (1996).

45.	Z. X. Liu, S. Pau, K. Syassen, J. Kuhl, W. Kim, H. Morkoç, M.A. Khan, and C.J. Sun, Phys. Rev. B **58**, 6696 (1998).

46.	S.L. Chuang and C.S. Chang, Phys. Rev. B **54**, 2491 (1996).

47.	G.B. Ren, Y.M. Liu, and P. Blood, J. Appl. Phys. **74**, 1117 (1999).

48.	R. Langer, J.Simon, V. Oritz, N.T. Pelekanos , A. Barski, R. Andre, and M.Godlewski, Appl. Phys.Lett. **74**, 3827 (1999).

49.	P. Lefebvre, J. Allegre, B. Gil, H. Mathieu, N. Grandjean, M. Leroux, J. Massies, and P. Bigenwald, Phys. Rev. B, **59**, 15363 (1999).

50.	R. Cingolani, A. Botchkarev, H. Tang, H. Morkoc, G. Traetta, G. Coli, M. Lomascolo, A. Di Carlo, F. Della Sala, and P. Lugli, Phys. Rev. B **61**, 2711 (2000).

51.	A. Thamm, O. Brandt, J. Ringling, A. Trampert, K.H. Ploog, O. Mayrock, H.-J. Wunsche, and F. Henneberger, Phys. Rev. B **61**, 16025 (2000).

52.	M.E. Lines and A.M. Glass, *Principles and Applications of Ferroelectrics and Related Materials* (Clarendon Press, Oxford, 1977).

53.	W. Ludwig, Festkorperphysik, Akademische Verlagsgesellschaft, Wiesbaden, 1978.

54.	J.F. Nye, *Physical Properties of Crystals* (Oxford University Press, Oxford, 1957).

55.	P. Waltereit, O. Brandt, A. Trampert, H. T. Grahn, J. Menniger, M. Ramsteiner, M. Reiche, and K. H. Ploog, Nature **406**, 865 (2000).

56.	J. Brown, F. Wu, P.M. Petroff, and J.S. Speck, Appl. Phys. Lett. **84**, 690 (2004).

57.	K. Kim, W.R.L. Lambrecht, and B. Segall, Phys. Rev. B **56**, 7018 (1997).

58. I. Vurgaftman and J.R. Mayer, J. Appl. Phys. **94**, 3675 (2003).

59. C. Van de Walle, private communication (2004).

60. F. Bernardini, V. Fiorentini, and D. Vanderbilt, Phys. Rev. B **56**, R10024 (1997).

61. O. Ambacher, M. Eickhoff, A. Link, M. Hermann, M. Stutsmann, F. Bernandini, V. Fiorentini, Y. Smorchkova, J. Speck, U. Mishra, W. Schaff, V. Tilak, and L.F. Eastman, phys. stat. sol. (a) **195**, 3 (2003).

62. M.D. McCluskey, C.G. Van de Walle, L.T. Romano, B.S. Krusor, and N.M. Johnson, J. Appl. Phys. **93**, 4340 (2003).

63. See, e.g., the freeware program 1D Poisson/Schrodinger by G. Snider: http://www.nd.edu/~gsnider/

64. K. Seo and T. Mura, J. Appl. Mech. **46**, 568 (1979).

65. O. Brandt, P. Waltereit and K.H. Ploog, J. Phys. D **35**, 577 (2002).

Appendix IV

GaN quantum dot density control by rf-plasma molecular beam epitaxy

J. Brown
Materials Department, University of California, Santa Barbara, CA 93106-5050

F. Wu
NICP/JST ERATO, UCSB Group, University of California, Santa Barbara, CA 93106-5050

P. M. Petroff
Materials Department, University of California, Santa Barbara, CA 93106-5050

J. S. Speck[a)]
Materials Department and NICP/JST ERATO, UCSB Group, University of California, Santa Barbara, CA 93106-5050

We report on the growth of GaN quantum dots and the control of their density in the Stranski–Krastanov mode on AlN (0001) by rf-plasma molecular beam epitaxy at 750 °C. After depositing the equivalent of 2–3 ML GaN coverage, as limited by N fluence under Ga-droplet growth conditions, excess Ga was desorbed and Stranski–Krastanov islands formed under vacuum. We present the dependence of island density as a function of GaN coverage (for two growth rates: 0.10 and 0.23 ML/s), as estimated from atomic force microscopy and cross-sectional transmission electron microscopy. With a GaN growth rate of 0.23 ML/s, the island density was found to vary from less than $3.0 \times 10^8 - 9.2 \times 10^{10}$ cm^{-2} as the GaN coverage was varied from 2.2 (critical thickness) to 3.0 ML. For a GaN growth rate of 0.10 ML/s, the island density varied from 2.0×10^{10} to 7.0×10^{10} cm^{-2} over a GaN coverage range of 2.0–3.0 ML. For each growth rate, the GaN islands were found to be of nearly uniform size, independent of the quantum dot density. © *2004 American Institute of Physics.* [DOI: 10.1063/1.1645333]

The control of GaN quantum dot (QD) size and density is of great interest for the fabrication of QD devices and investigation of their physical properties. Low-density, size-controlled GaN QDs are necessary for the study of spatially isolated QDs by techniques such as cathodoluminescence and microphotoluminescence without the need for metal masks or etched mesas. Higher densities of GaN QDs are potentially useful to improve the efficiency of active regions for optoelectronics applications for emission of ultraviolet to blue light.

Several groups have demonstrated control of GaN QD growth by metalorganic chemical vapor deposition (MOCVD) and molecular beam epitaxy (MBE).[1–4] In rf-plasma MBE of GaN on AlN (0001) at 750 °C, it has been shown that above 2.5 ML coverage, GaN will transition from a coherently strained two-dimensional (2D) layer to the Stranski–Krastanov (SK) configuration [coherently strained 2D wetting layer plus three-dimensional (3D) islands].[3] Simultaneous size and limited density control has also been demonstrated; small, high-density SK islands have been ripened under N flux or vacuum to produce larger, low-density islands.[4] Recently, significant progress has been made toward understanding the surfactant effect of excess Ga in thin film GaN growth (under a dynamically stable Ga adlayer) on AlN (0001) by rf-plasma MBE.[3,5] Despite recent progress in control of the growth of GaN QDs by rf-plasma MBE, the lowest reported density of MBE-grown GaN QDs is 4

$\times 10^{10}$ cm^{-2} at 3 ML of GaN coverage.[3] In this work, we report growth of GaN QDs by plasma-assisted MBE with densities from 3.0×10^8 to 9.2×10^{10} cm^{-2} via control of N-limited GaN coverage prior to the SK transition. We show that the density of GaN QDs may be varied, nearly independent of mean GaN QD size, via N-fluence control under Ga-rich conditions.

Growths were performed in an Applied EPI Gen II MBE system, equipped with conventional Al and Ga Knudsen effusion cells and a standard Unibulb nitrogen rf-plasma sources. We used *ex situ* high-resolution x-ray diffraction of GaN/Al$_{0.1}$Ga$_{0.9}$N superlattices grown on ~2-μm-thick MOCVD-GaN template to calibrate the N-limited GaN growth rate corresponding to 150 W rf-plasma forward power and 0.2–0.4 sccm nitrogen flow. Radial (ω-2θ), triple-axis x-ray diffraction scans about GaN (0002) were compared to dynamical simulations[6] to correlate layer thickness, grown under Ga-droplet conditions, to deposition time. The N-limited growth rate uncertainty ($\pm 1\%$, typical) determined for each superlattice sample by this method was less than the overall fluctuation of the growth rate ($\pm 1.9\%$) for separate sample growths within the two growth rates used in this study.

GaN QDs were grown at 750 °C by rf-plasma MBE on partially relaxed 100 nm AlN buffers on ~2-μm-thick MOCVD-GaN on sapphire. AlN was grown under slightly metal-rich conditions ($f_{Al}/f_N \sim 1.1$). Before GaN deposition, excess Al was consumed under N flux exposure (i.e., producing AlN). The AlN surfaces were simultaneously exposed to Ga and N flux ($4 < f_{Ga}/f_N < 8$), in the Ga-droplet regime at 750 °C.[7] Under these conditions, the nominal GaN coverage

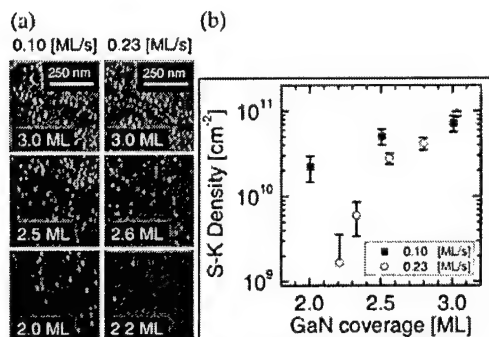[a)]Author to whom correspondence should be addressed; electronic mail: speck@mrl.ucsb.edu

FIG. 1. SK island density for various GaN coverages for two GaN growth rates. (a) AFM (amplitude) micrographs of GaN SK surfaces. (b) GaN SK island density as a function of GaN coverage. Error bars indicate standard deviation from separate measurements.
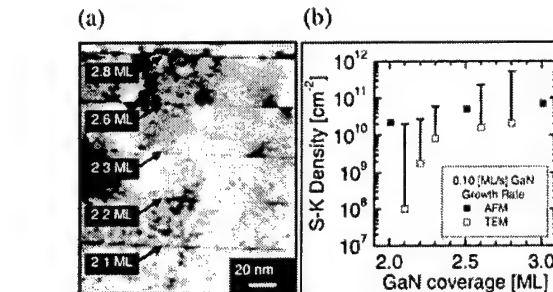

FIG. 2. (a) Cross section TEM micrograph of a stack of GaN SK islands (QDs) with varying GaN coverage in AlN (0001). (b) Estimated density of SK islands as a function of GaN coverage by AFM and TEM. Error bars are one standard deviation.

was specified by the supplied active N flux, which is understood to diffuse rapidly on or through the excess Ga ad layer(s). The morphological evolution of the surfaces was then observed via reflection high-energy electron diffraction (RHEED) along the $[11\bar{2}0]$ azimuth under vacuum. Above 2.0 ML nominal GaN coverage, we observed the concurrent desorption of excess Ga and the onset of the GaN SK transition after 5–20 s as evidenced by the RHEED transition from 2D diffraction surface normal streaks to 3D diffraction Bragg spots.[3,8] The samples were either cooled immediately and studied by atomic force microscopy (AFM), or overgrown with AlN for examination by cross-section transmission electron microscopy (TEM).

We used AFM to characterize GaN SK islands on partially relaxed AlN buffers. In a series of ~ 1 cm^2 samples for two growth rates (0.10($\pm$1.9%) and 0.23($\pm$1.9%) ML/s), we observed a strong correlation between island density and GaN coverage from 2.0 to 3.0 ML (Fig. 1). Independent of growth rate, the island density saturated at $\sim 9 \times 10^{10}$ cm^{-2} at 3.0 ML GaN coverage. Below 3.0 ML coverage, the 0.10 ML/s growth rate series had higher island densities than the 0.23 ML/s series. The opportunity for increased N diffusion (under excess Ga) prior to the SK transformation at the lower growth rate may provide for enhanced diffusion of adatoms to stable island nucleation sites. This effect may account for higher island density at a given coverage for the lower growth rate series. The difference between the island density trends for the two series may also be a result of Ga *fluence*. The Ga flux (1×10^{-6} beam equivalent pressure) and substrate temperature (750 °C) were held constant for both growth rate series; the 0.10 ML/s series was exposed to approximately two times greater Ga fluence during the GaN deposition under Ga-droplet conditions. Under our growth conditions, the GaN surface was initially smooth under adsorbed excess Ga, and subsequently evolved into the SK configuration as the excess Ga desorbed. The delay after GaN deposition, but before the SK transition, during which N is able to diffuse rapidly, may be critical in the transition from the (metastable) coherently strained 2D layer to the partially relaxed SK configuration.

Within the limits of AFM measurement, the mean GaN SK island heights and diameters were nearly independent of the island density for each growth rate. As the GaN coverage was varied from 2.2 to 3.0 ML (GaN growth rate: 0.23 ML/

s), the mean island height exhibited a modest increase (12%), from 2.5$\pm$0.7 to 2.8$\pm$0.6 nm. Over the same range of GaN coverage, the SK island height distributions remained large (standard deviations 20%–30% of mean height) independent of island density. The mean island diameter (full width at half maximum) for the 0.23 ML/s series was also nearly independent of coverage, exhibiting an overall mean of 11 $\pm$7 nm. For the lower growth rate (0.10 ML/s) series, the mean island height was 2.4$\pm$0.7 nm, and the mean island diameter was 16$\pm$7 nm. The QD sizes and densities obtained from AFM measurements were used to estimate the amount of GaN contained in the SK islands, assuming a lens (spherical cap) island shape. For both growth rates, the amount of GaN contained in the islands was equivalent to the excess (above critical thickness for the SK transition) GaN deposited. This indicates that after GaN deposition under Ga droplet conditions, the excess Ga desorbs, but the supplied N fluence remains on the surface during the SK transition. The critical thickness for the 0.23 ML/s series was 2.2 ML, and for the 0.10 ML/s series the critical thickness was apparently less than 2.0 ML. Our results indicate a GaN (2D) "wetting layer" of approximately 2 ML is formed initially, followed by the formation of SK islands with excess GaN.

To verify the control of GaN QD density (GaN SK islands immediately covered by AlN) as a function of GaN coverage, a multilayer stack of GaN QDs was examined by two-beam TEM. The GaN coverage was varied from 2.1 to 2.8 ML, (growth rate: 0.10 ML/s), with 30 nm AlN spacer layers. The dependence of QD density on coverage was consistent with the relationship found on the uncapped GaN SK surfaces (Fig. 2).

For moderate to high GaN coverage (above 2.5 ML), the surfaces of individual ~ 1 cm^2 samples exhibited nearly uniform island density. The surface of a ~ 1 cm^2 sample (growth rate 0.23 ML/s; coverage 2.2 ML) had a maximum island density of 1.2×10^{10} cm^{-2} and a minimum density of 3×10^8 cm^{-2}. A contour plot of this surface (Fig. 3) was generated by the use of a correlation method to grid nine individual island density data points into a 3×3 matrix. The island density *decreased* in the direction defined by the impinging N plasma flux. The amount of available N (sticking coefficient ~ 1 under excess Ga conditions)[7,9] for GaN growth is expected to decrease along the direction of N impingement, consistent with our correlation of SK island density to GaN coverage as determined by the supplied active
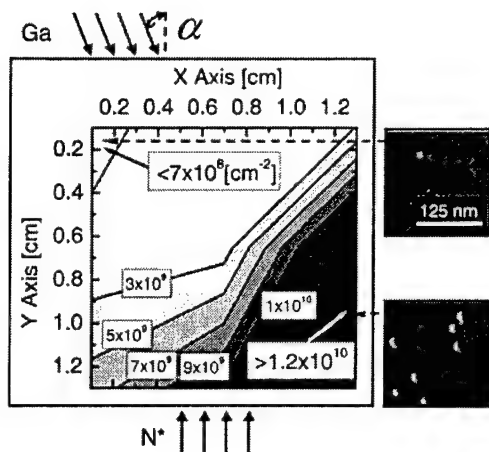
FIG. 3. SK island density on the surface of a 2.2 ML GaN coverage sample (GaN growth rate: 0.23 ML/s). Approximate Ga and N* flux sample-plane impingement directions are shown schematically ($\alpha=45°$). Representative AFM (amplitude images) depict the highest and lowest island density regions.

nitrogen. The SK island density *increased* in the direction defined by the impinging Ga flux, consistent with the proposed role of Ga as a surfactant for GaN growth on AlN (0001).[5] On this sample, the lowest island density (3 $\times 10^8$ cm^{-2}) was observed near the highest Ga flux and the lowest N flux, while the highest island density (1.2 $\times 10^{10}$ cm^{-2}) was observed near the lowest Ga flux and the highest N flux.

In conclusion, we have demonstrated a route for control of GaN QD density over more than two orders of magnitude, by control of the GaN coverage and growth rate. We found that the GaN QD density may be controlled nearly independent of QD size.

[1] S. Tanaka, S. Iwai, and Y. Aoyagi, Appl. Phys. Lett. **69**, 4096 (1996).
[2] M. Miyamura, K. Tachibana, T. Someya, and Y. Arakawa, J. Cryst. Growth **237–239**, 1316 (2002).
[3] C. Adelmann, N. Gogneau, E. Sarigiannidou, J.-L. Rouviere, and B. Daudin, Appl. Phys. Lett. **81**, 3064 (2002).
[4] B. Daudin, F. Widmann, G. Feuillet, Y. Samson, M. Arlery, and J. L. Rouviere, Phys. Rev. B **56**, R7069 (1997).
[5] G. Mula, C. Adelmann, S. Moehl, J. Ouillier, and B. Daudin, Phys. Rev. B **64**, 195406 (2001).
[6] O. Brandt, P. Waltereit, and K. Ploog, J. Phys. D **35**, 577 (2002).
[7] B. Heying, R. Averbeck, L. F. Chen, E. Haus, H. Riechert, and J. S. Speck, J. Appl. Phys. **88**, 1855 (2000).
[8] J. Brown, C. Elsass, C. Poblenz, P. M. Petroff, and J. S. Speck, Phys. Status Solidi B **228**, 199 (2001).
[9] C. Adelmann, J. Brault, D. Jalabert, P. Gentile, H. Mariette, and G. Mula, J. Appl. Phys. **91**, 9638 (2002).

Appendix V

Continuous evolution of Ga adlayer coverages during plasma-assisted molecular beam epitaxy of (0001) GaN

G. Koblmüller [a)]
Infineon Technologies AG, Corporate Research Photonics, D-81730 Munich, Germany,
and Institute of Solid State Physics, Vienna University of Technology, A-1040 Vienna, Austria

J. Brown
Materials Department, University of California, Santa Barbara, CA 93106-5050, U. S. A.

R. Averbeck and H. Riechert
Infineon Technologies AG, Corporate Research Photonics, D-81730 Munich, Germany

P. Pongratz
Institute of Solid State Physics, Vienna University of Technology, A-1040 Vienna, Austria

J. S. Speck
Materials Department, University of California, Santa Barbara, CA 93106-5050, U. S. A.

Corresponding author: Gregor Koblmüller

Infineon Technologies
Corporate Research, Photonics Division
Otto-Hahn-Ring 6
D-81739 Munich
Germany
Phone: ++49-89-234-48923
Fax: ++49-89-234-53294
Electronic mail: Gregor.Koblmueller@infineon.com

Abstract

We present a study of the evolution of the Ga adlayer during plasma–assisted molecular beam epitaxy of (0001) GaN as a function of both Ga flux and growth temperature. In situ quadrupole mass spectrometry was used to quantitatively determine the adsorbed Ga coverage by monitoring its subsequent desorption after GaN growth. Independent of the growth time, the Ga adlayer was found to form steady state coverages that increase *continuously* from 0 to 2.5 monolayers when raising the Ga flux from N–rich to moderate Ga–rich growth conditions. At higher Ga fluxes or lower growth temperatures (Ga droplet regime), macroscopic Ga droplets form on top of the Ga adlayer. Based on the temperature–dependency for the transition between the Ga adlayer and Ga droplet regime we determined an apparent activation energy of 3.4 eV, which is discussed with respect to previously reported values.

With its importance as a material enabling the fabrication of optoelectronic[1-3] and high–power[4] electronic devices, GaN has become subject to an increasing number of fundamental research studies on the physical issues of nitride growth. In plasma–assisted molecular beam epitaxy (PAMBE), several studies have highlighted the important role of the Ga/N flux ratio and the growth temperature, i.e. growth kinetics, on the growth mode and resulting surface structure of GaN films, which in turn determine their structural, electrical and optical properties.[5-13] Specifically, GaN grown with low Ga/N ratios (N–rich growth) results typically in heavily pitted surfaces, a tilted columnar structure with a high density of stacking faults[6] and insulating material[9]. High Ga/N ratios (Ga–rich growth) prove necessary to acquire device quality GaN through a two–dimensional growth mode.[5] Systematic morphology studies revealed a gradual reduction in surface pit density as the Ga/N ratio was increased from N–rich to Ga–rich droplet conditions.[9,10] Similarly, the electron mobility in (0001) GaN[9] and two-dimensional electron gas (2DEG) AlGaN/GaN structures[14] was found to increase with rising Ga/N ratio and reaches its highest values at a Ga/N ratio marginally below the border for Ga droplet formation. Restrictions for device applications, however, were shown to arise for very high Ga/N ratios or low temperatures, as these lead inevitably to the accumulation of metallic Ga droplets on the surface.[10]

A full understanding of these kinetically-driven differences relies heavily on the GaN surface atomic structure during growth and its effect on adatom diffusion and incorporation mechanisms prevailing in the various growth regimes. Recent theoretical[15,16] and experimental[12,16-18] studies found that under Ga–rich conditions the (0001) GaN growth front is stabilized by a metallic Ga adlayer, which is absent during N–rich growth. Such a Ga adlayer facilitates high adatom mobilities[19], particularly fostering adatom transport between subsurface sites (the so–called autosurfactant effect).[20] High adatom diffusion rates under Ga droplet growth conditions were further employed to reduce the areal density of self-assembled GaN quantum dots to below 5×10^8 cm^{-2}.[21]

To explore adatom mobility and the resulting GaN material properties, extensive efforts have been made to quantify the Ga adlayer coverage as a function of the growth conditions. So far, the only *in situ* studies were based upon determining the desorption time of the Ga adlayer from measurements of specular beam intensities in reflection high energy electron diffraction (RHEED) patterns.[13,22] With the assumption of a constant desorption rate, i.e. a linear relationship between desorption time and Ga adlayer coverage, the latter was then proposed to evolve *discontinuously* with increasing Ga flux and to form a stable ≈ 2.5 mono-layer (ML) bilayer for a wide range of Ga fluxes. Such self-regulated discrete Ga adlayer coverages would then be expected to produce constant material properties despite small fluctuations in substrate temperature or Ga flux.

In this letter, we present a quantitative description of the Ga adlayer coverage during PAMBE growth of (0001) GaN by employing line–of–sight quadrupole mass spectrometry (QMS) as a direct method to monitor the desorbing Ga atoms. Based on our previously reported *non-constant* Ga adlayer desorption rate[18], we demonstrate that with rising Ga flux the Ga adlayer forms steady state coverages that increase *continuously* from zero up to 2.5 ML during GaN growth. Therefore, no evidence of self-regulating Ga coverage is found which means that precise control of Ga/N ratio and growth temperature is required to stabilize the growth conditions for optimum material properties.

The experiments were carried out in a MBE system equipped with standard Ga effusion cells and an EPI Unibulb radio frequency plasma source supplied with reactive nitrogen of >5N purity (99.999%). The substrates used were ≈2-μm–thick GaN (0001) templates grown by metalorganic chemical vapor deposition (MOCVD) on *c*–plane sapphire wafers. The substrate temperature was measured by a pyrometer with a maximum sensitivity at 940 nm. The offset between the pyrometer temperature and the actual GaN surface temperature was estimated by the measurement of the critical temperature to form Ga droplets on GaN with a calibrated Ga

flux. Radiative substrate heating was facilitated by coating the backside of the substrates with TiW (a refractory metal). We present molecular fluxes in terms of potential GaN growth rate in units of ML/sec, as determined from thickness measurements of GaN samples grown under Ga– and N–rich conditions.[10] Growths were performed with a fixed nitrogen flux of 0.23 ML/sec, while the Ga flux was varied from 0.06–2.25 ML/sec for a temperature set ranging from 669 to 734 °C. To monitor the desorbing Ga atoms a quadrupole mass spectrometer was installed in direct line of sight to the wafer. We calibrated the desorbing Ga flux by determining the partial pressure of the ^{69}Ga isotope for a sequence of known Ga fluxes evaporated onto a sapphire substrate at such a high temperature ($\approx$800 °C) so that all impinging Ga completely desorbed.[18,23] With the acquired linear relationship of 1.9×10^{-10} mbar/ML sec^{-1} we were thus able to quantify the desorbing Ga in units of ML.

Ga desorption measurements for a series of 90 sec GaN growth pulses with varying Ga fluxes at a temperature of 722 °C are presented in Fig. 1(a). In relation to the GaN growth diagram, the Ga flux was varied from the Ga droplets regime to N-Rich flux conditions in order to maintain (by applying the Ga autosurfactant effect[12]) a smooth non–disrupted GaN growth front for subsequent growth pulses. Each GaN growth pulse provides two phases in the desorbed Ga signal, one during growth itself (later referred to as the maximum desorption level) and the other as vacuum desorption of an adsorbed Ga surface coverage after growth [also detailed in the closeup views of Fig. 1 (b) and (c) for two different Ga fluxes]. According to the maximum desorption level in the growth phase, we can differentiate – as in our previous study[10] – between three distinct regimes of growth: for high Ga fluxes between 1.93 and 1.22 ML/sec (A) the maximum desorption is constant at a rate around 1 ML/sec. This rate is limited by the temperature and any excess Ga flux accumulates as weakly–bonded metallic droplets on the surface (Ga droplet regime).[18] When the Ga flux is lowered to a range between 1.22 – 0.23 ML/sec (B) the maximum desorption level decreases monotonically. This is referred to the Ga–rich intermediate regime, where the excess Ga flux desorbs from the

growing surface (independent of the supplied flux). And third, GaN growth with Ga fluxes below 0.23 ML/sec (C) results in virtually no Ga desorption, since the arriving Ga flux limits the growth rate and is consumed completely by the nitrogen atoms (N-rich regime).[5]

To evaluate the Ga surface coverage prevalent in the different regimes, we integrated the area below the desorbing Ga flux during the vacuum desorption of each pulse [i.e. hatched area as exemplified in Fig. 1(b) and (c); a detailed description of the desorption behavior can be found elsewhere[18]]. The integrated Ga coverages are plotted in Fig. 2 as a function of the impinging Ga flux (full circles), which demonstrate a *continuous* increase of the Ga surface coverage with increasing Ga flux. For N–rich growth, no excess Ga is accumulated on the surface, but Ga–rich intermediate conditions yield Ga adlayer coverages between 0 and 2.5 ML. Within the intermediate regime error bars are on the order of ± 0.3 ML, resulting from the 2 sec time resolution of the mass spectrometer. However, for the lower investigated temperatures of 669 °C and 686 °C the respective error is only ± 0.1 ML, due to the greater duration of the Ga adlayer desorption process. From additional growth experiments with growth times up to 2 hours we observed that these adlayer coverages did not vary more than ± 0.2 ML for any given Ga flux, hence being completely independent of the previous growth time. Thus, for each Ga flux a certain steady–state coverage is stabilized within the intermediate regime. The maximum Ga adlayer coverage of 2.5 ML measured in this work is in good agreement with the laterally–contracted bilayer model (i.e. 2.33 ML of Ga in terms of GaN atomic density), which was calculated to be the energetically most favorable surface structure under Ga-rich conditions.[15] For very high Ga fluxes, the slope in Ga surface coverage changes drastically, which is attributed to an increasing accumulation of Ga droplets on top of the bilayer.[13,22] For comparison, we have also evaluated the desorption time of the Ga surface coverage, given by the duration between the closure of both Ga and N shutters and the drop to zero desorption (open circles in Fig. 2). The desorption time evolves in contrast to the Ga surface coverage; it shows two constant plateaus for Ga fluxes in the range between

0.4 – 1.22 ML/sec (error bars are ± 2 sec). This can be understood by a *non-constant desorption rate*, which we have previously determined for Ga adlayer coverages between 1 – 2.4 ML.[18] Particularly, the decay of the Ga bilayer was found to consist of a complicated three-stage desorption process, and only submonolayer coverages desorb in a monoexponential fashion. At this stage it becomes clear why we observe a continuous increase in the Ga adlayer coverage with rising Ga flux, in constrast to apparent regimes of constant coverages as evaluated from changes in RHEED intensity by Adelmann et al.[13,22] The continuous behavior has also been strongly anticipated in recent morphology and electron mobility studies of thick GaN films.[9,10]

The explicit relationship between impinging Ga flux and steady–state Ga surface coverage has also been verified for different temperatures [Fig. 3]. As a clear trend, with higher growth temperatures the transition between Ga adlayer and Ga droplet coverages is shifted to higher Ga fluxes, whereas the stoichiometry border (where Ga and N fluxes are equal) is independent of the temperature. Moreover, taking the transition fluxes between the intermediate and droplet regime, given by the intersection at 2.5 ML, as a function of temperature yields an Arrhenius dependence with an apparent activation energy that we determined to be 3.4 ± 0.1 eV. Our recent Ga desorption observations without N yielded activation energies of 3.1 and 3.7 eV for the desorption of Ga droplets and the top part of the bilayer, respectively.[18] Hence, the value of 3.4 eV for the current phase transition fits favorably within the two and supports our previous study. Much higher activation energies for this particular transition have been reported from RHEED intensity measurements, being 4.8 eV (Ref. 13) with incident N and 5.1 eV (Ref. 22) without N. Lower values of around 2.8 eV resulted from our earlier investigation[10] as well as from RHEED transitions between 2×2 and 1×1 reconstructed surfaces[24]. In both of these latter studies the supplied N fluxes were substantially higher, which could be responsible for the different outcomes in the activation energies. On the basis of first–principles total energy calculations it was proposed that there

might be a strong interdependency between N flux and a temperature–dependent Ga bilayer coverage that in turn could influence the activation energy for the nucleation of Ga droplets.[22] However, the current QMS results reveal that independent of the growth temperature (at least in the investigated range) the contracted Ga bilayer coverage is constant at 2.5 ± 0.2 ML within the experimental limits.

In conclusion, line–of–sight quadrupole mass spectrometry has proved a powerful *in situ* method to quantitatively determine the adsorbed Ga surface coverages during MBE growth of (0001) GaN. In contrast to the present perception of step–wise coverages, we demonstrated by direct observation that the steady–state Ga coverage increases *continuously* with rising Ga flux from zero coverage at the stoichiometry border to a laterally contracted $\approx$ 2.5 ML thick bilayer configuration at the Ga droplet border. As the Ga adlayer governs the adatom mobility, this monotonic behavior is also directly reflected in consequent GaN material properties, as will be discussed in a forthcoming paper.[25] In addition, the continuous evolution and the maximum $\approx$ 2.5 ML adlayer coverage are independent of the growth temperature, but the onset for Ga droplet formation was found to follow a clear Arrhenius dependency with an apparent activation energy of 3.4 eV.

[1] S. Nakamura, T. Mukai, and M. Senoh, Appl. Phys. Lett. **64**, 1687 (1994).

[2] H. Tews, R. Averbeck, A. Graber, and H. Riechert, Electron. Lett. **32**, 2004 (1996).

[3] R. P. Vaudo, I. D. Goepfert, T. D. Moustakas, D. M. Beyea, T. J. Frey, and K. Meehan, J.
Appl. Phys. **79**, 2779 (1996).

[4] U. K. Mishra, Y.-F. Wu, B. P. Keller, S. Keller, and S. P. DenBaars, in *Physics of
Semiconductor Devices*, edited by V. Kumar and S.K. Agarwal (Narosa, New Delhi 1998),
and references therein.

[5] H.Riechert, R. Averbeck, A. Graber, M. Schienle, U. Strauß and H. Tews, Mat. Res. Soc.
Symp. Proc. **449**, 149 (1997).

[6] E. J. Tarsa, B. Heying, X. H. Wu, P. Fini, S. P. Den Baars, and J. S. Speck, J. Appl. Phys. **82**,
5472 (1997).

[7] S. Einfeldt, U. Birkle, C. Thomas, M. Fehrer, H. Heinke, and D. Hommel, Mat. Sci. Eng. **B
50**, 12 (1997).

[8] B. Heying, E. J. Tarsa, C. R. Elsass, P. Fini, S. P. Den Baars, and J. S. Speck, J. Appl. Phys.
85, 6470 (1999).

[9] B. Heying, I. Smorchkova, C. Poblenz, C. Elsass, P. Fini, S. P. Den Baars, U. Mishra and J.
S. Speck, Appl. Phys. Lett. **77**, 2885 (2000).

[10] B. Heying, R. Averbeck, L. F. Chen, E. Haus, H. Riechert, and J. S. Speck, J. Appl. Phys.
88, 1855 (2000).

[11] V. Ramachandran, C. D. Lee, R. M. Feenstra, A. R. Smith, J. E. Northrup, and D. E. Greve,
J. Cryst. Growth **209**, 355 (2000).

[12] G. Mula, C. Adelmann, S. Moehl, J. Oullier, and B. Daudin, Phys. Rev. B **64**, 195406 (2001).

[13] C. Adelmann, J. Brault, D. Jalabert, P. Gentile, H. Mariette, G. Mula, and B. Daudin, J. Appl. Phys. **91**, 9638 (2002).

[14] C. R. Elsass, C. Poblenz, B. Heying, P. Fini, P. M. Petroff, S. P. DenBaars, U. K. Mishra, and J. S. Speck, J. Cryst. Growth **233**, 709 (2001).

[15] J. E. Northrup, J. Neugebauer, R. M. Feenstra, and A. R. Smith, Phys. Rev. B **61**, 9932 (2000).

[16] A. R. Smith, R. M. Feenstra, D. W. Greve, M.-S. Shin, M. Skowronski, J. Neugebauer, and J. E. Northrup, J. Vac. Sci. Technol. B **16**, 2242 (1998).

[17] S. H. Xu, H. Wu, X. Q. Dai, W. P. Lau, L. X. Zheng, M. H. Xie, and S. Y. Tong, Phys. Rev. B **67**, 125409 (2003).

[18] G. Koblmüller, R. Averbeck, H. Riechert, and P.Pongratz, Phys. Rev. B **69**, 035325 (2004).

[19] T. Zywietz, J. Neugebauer, and M. Scheffler, Appl. Phys. Lett. **73**, 487 (1998).

[20] J. Neugebauer, T. Zywietz, M. Scheffler, J. E. Northrup, H. Chen, and R. M. Feenstra, Phys. Rev. Lett. **90**, 056101 (2003).

[21] J. Brown, F. Wu, P. M. Petroff, and J. S. Speck, Appl. Phys. Lett. **84**, 690 (2004).

[22] C. Adelmann, J. Brault, G. Mula, B. Daudin, L.Lymperakis, and J. Neugebauer, Phys. Rev. B **67**, 165419 (2003).

[23] G. Koblmüller, P. Pongratz, R. Averbeck, and H. Riechert, Appl. Phys. Lett. **80**, 2281 (2002).

[24] P. Hacke, G. Feuillet, H. Okumura, and S. Yoshida, Appl. Phys. Lett. **69**, 2507 (1996).

[25] J. Brown, G. Koblmüller, R. Averbeck, H. Riechert, P. Pongratz, and J. S. Speck

(unpublished).

FIGURE CAPTIONS

FIG. 1. (a) Ga desorption for a series of 90 sec GaN pulses with gradually decreasing Ga fluxes from 1.93 – 0.06 ML/sec at constant 722°C. The Ga fluxes in the (b) droplet and (c) intermediate regimes illustrate the determination of the Ga surface coverage (equal to the hatched areas) from its vacuum desorption after growth.

FIG. 2. Evolution of the Ga surface coverage and its characteristic desorption time as a function of the impinging Ga flux for (0001) GaN growth at constant N flux (0.23 ML/sec) and T = 722 °C. Error bars for the surface coverage are ± 0.3 ML and ± 2 sec for the desorption time, respectively.

FIG. 3. Temperature–dependent Ga surface coverages as a function of the impinging Ga flux, yielding a transition between Ga adlayer and droplet fluxes with an Arrhenius nature and an activation energy of 3.4 ± 0.1 eV.
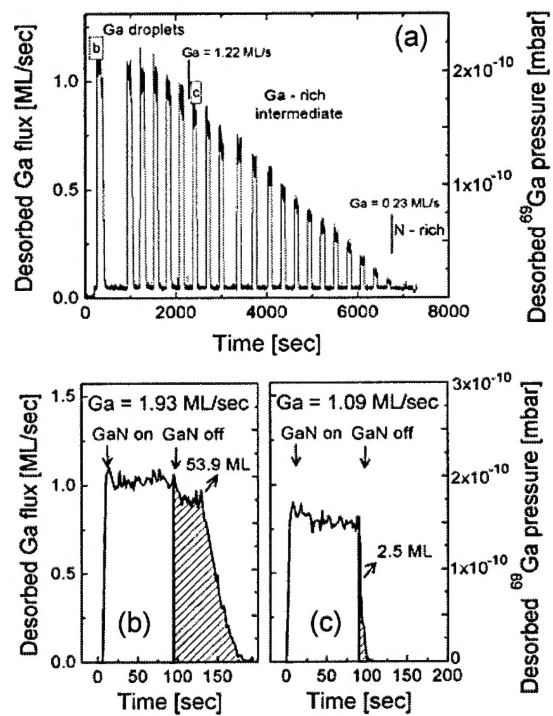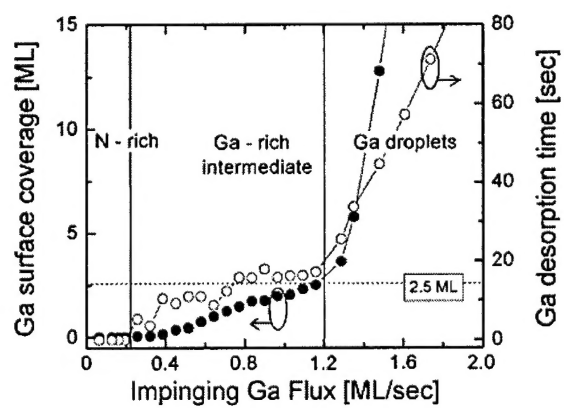
Fig. 1/3

G. Koblmüller

Fig. 2/3

G. Koblmüller

Fig. 3/3
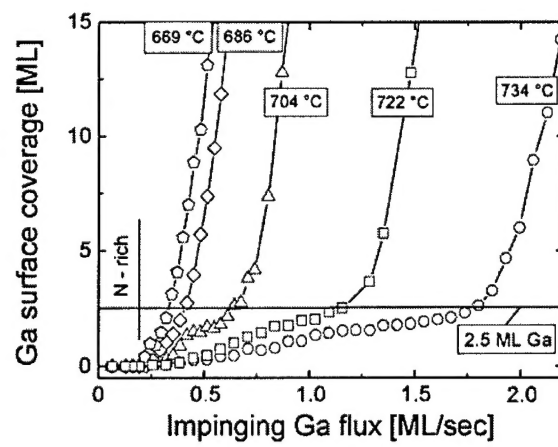
G. Koblmüller